The Asymmetric Thick Disk: A Star Count and Kinematic Analysis. II The Kinematics

Jennifer E. Parker[1], Roberta M. Humphreys[1]

Department of Astronomy, University of Minnesota, Minneapolis, MN 55455

parker@astro.umn.edu

roberta@aps.umn.edu

and

Timothy C. Beers

Department of Physics and Astronomy, Michigan State University, East Lansing, MI 48824

beers@pa.msu.edu

Received _____; accepted _____

Submitted to the Astronomical Journal

[1]Visiting Astronomer, Kitt Peak National Observatory and Cerro Tololo Inter-American Observatory, National Optical Astronomy Observatory, which is operated by the Association of Universities for Research in Astronomy, Inc. (AURA) under cooperative agreement with the National Science Foundation.

ABSTRACT

We report a kinematic signature associated with the observed asymmetry in the distribution of thick disk/inner halo stars interior to the Solar circle described in Paper I. In that paper we found a statistically significant excess (20 – 25%) of stars in quadrant I ($l \sim 20°$ to $55°$) both above and below the plane ($b \sim \pm\ 25°$ to $\pm\ 45°$) compared to the complementary region in quadrant IV. We have measured Doppler velocities for 741 stars, selected according to the same magnitude and color criteria, in the direction of the asymmetry and in the corresponding fields in quadrant IV. We have also determined spectral types and metallicities measured from the same spectra. We not only find an asymmetric distribution in the V_{LSR} velocities for the stars in the two regions, but the angular rate of rotation (ω) for the stars in quadrant I reveals a slower effective rotation rate compared to the corresponding quadrant IV stars. The results for V_{LSR} and ω also show an interesting dependence on Galactic longitude which is most pronounced in quadrant I. We use our [Fe/H] measurements to separate the stars into the three primary population groups, halo, thick disk, and disk, and conclude that it is primarily the thick disk stars that show the slower rotation in quadrant I. These stars are also responsible for the observed variation of V_{LSR} and ω with Galactic longitude. A solution for the radial, tangential and vertical components of the V_{LSR} velocities, reveals a significant lag of $\approx$ 80 to 90 km s^{-1} in the direction of Galactic rotation for the thick disk stars in quadrant I, while in quadrant IV, the same population has only a $\sim$ 20 km s^{-1} lag confirming the kinematic asymmetry between the two directions. In Paper I we concluded that the asymmetry in the star counts could be best explained by either a triaxial thick disk or an interaction between the bar in the disk and the thick disk/inner halo stars. The results reported here support a rotational lag among the thick disk stars due

to a gravitational interaction with the bar as the most likely explanation for the asymmetry in both the star counts and the kinematics. The affected thick disk stars, however, may be associated with the recently discovered Canis Major debris stream or a similar merger event.

Subject headings: galaxy: structure: stellar content: halo: kinematics

1. Introduction

In Parker *et al.* (2003), hereafter Paper I, we reported evidence for an asymmetrical excess of thick disk/inner halo stars extending from approximately $l \sim 20°$ to $55°$ and $b \sim 25°$ to $45°$ both above and below the plane. In Paper I we considered three possible explanations for the asymmetry, including a possible merger remnant, but concluded that either a triaxial thick disk (Blitz & Spergel 1991), with its major axis in quadrant I or an interaction with the bar in the disk (Hernquist & Weinberg 1992; Debattista & Sellwood 1998) best explained the observations. Both of these would explain the star count excess but with different kinematics. A triaxial thick disk/inner halo, for example, may have a distinct rotational velocity about the Galactic center different from the disk. Indeed thick disk stars are observed to have a lag of 30-50 km s^{-1} (Reid 1998; Chiba & Beers 2000) with respect to disk stars. However a fast rotating bar in the disk in quadrant I with co-rotation at 3–4 kpc from the Galactic center could induce a gravitational "wake" that would trap and pile up stars behind it (Hernquist & Weinberg 1992; Debattista & Sellwood 1998). In response to the bar, there would not only be an excess of stars, but some of the stars might show a measurable "lag" or slower rotation as a result. Thus in either case, if the asymmetry in the star counts is due to a structural feature, then it should be supported by an asymmetrical pattern in the stars' motions. To search for a kinematic signature associated with the asymmetry in the star counts that could also provide additional

evidence for the cause of the asymmetry, we have obtained medium resolution spectra for radial velocities, spectral classification, and metallicity estimates of stars selected from 12 fields, 6 each in the direction of the asymmetry feature and in the corresponding regions in quadrant IV.

In §2 and §3 we briefly describe the observations and data reduction. In §4, we discuss the velocities, spectral classification, metallicity estimates, and evidence for a population dependent asymmetry. In the final section we summarize the results of our kinematics analysis and its implications for the origin of the observed asymmetry.

2. The Observations and Field and Object Selection

We used HYDRA, a multi-object spectrometer on the Blanco 4–meter at Cerro Tololo Interamerican Observatory (CTIO), and on the WIYN[2] 3.5–meter at Kitt Peak National Observatory (KPNO). Each HYDRA instrument has two sets of fiber bundles. WIYN-HYDRA has red and blue bundles with a $60'$ field-of-view, and we used the $3\farcs1$ diameter blue fibers which cover wavelengths from 3000-7000Å. CTIO-HYDRA is an upgrade from WIYN-HYDRA with 40 additional fibers and faster fiber configuration. CTIO-HYDRA has a $40'$ field of view and two fiber bundles, one with $1\farcs3$ apertures and a large bundle with $2\farcs0$ apertures. Unlike WIYN-HYDRA, both fiber bundles cover the spectral range 3000-11,000Å. CTIO-HYDRA has the advantage of smaller fibers for more precise positioning and to potentially acquire dimmer objects. At the time of our observations, CTIO-HYDRA had just been commissioned and had not yet been upgraded to the 400 mm Bench Schmidt camera with a SiTe 2×4K array, but instead was used with

[2]The WIYN Observatory is a joint facility of the University of Wisconsin-Madison, Indiana University, Yale University, and the National Optical Astronomy Observatory.

the 229mm Air Schmidt camera with a Loral 1 × 3K engineering array. This configuration prevented the use of all 138 large fibers, and to prevent the spectra from overlapping, we used every other fiber. Table 1 summarizes the characteristics of the CTIO and KPNO HYDRA spectrometers. Both instrument configurations had a resolution of 1Å per pixel. Further information regarding the specifics of the instruments can be found at http://www.noao.edu/ctio/ or http://www.noao.edu/kpno/wiyn/.

We selected stars from four fields with a strong star count excess and two transition fields in quadrant I (Paper I) and their complementary matched fields in l and b in quadrant IV. Figure 1 shows the distribution of the POSS I fields observed and at which observatory the observations were made. Using the Minnesota APS Catalog of the POSS I (http://aps.umn.edu), we randomly selected stars between O magnitude 16 and 18 with colors between the peak of the color–magnitude distribution, $(O-E)_{peak}$ near $(O-E) = 1.0$ mag, and $[(O-E)_{peak}$ - 1] mag[3]. The contribution of the halo and thick disk stars to the star counts is expected to be more than 80% (Paper I) in this magnitude and color range. For the CTIO fields, the $40'$ diameter central region of each plate was queried. For the WIYN fields we were able to use a slightly larger $60'$ diameter region. Each star was checked against known catalogs to eliminate any high proper motion stars. To prepare for the observations, we used a simulator to manually place each usable fiber on a star, a guide star or a blank sky field. The instrument requires that there be 4 to 5 FOPS stars, or bright guide stars of ≈ 10th magnitude, and for WIYN-HYDRA these stars had to be located near the edges of the field. As a result of the precise APS astrometry, we were able to easily acquire every guide star and the target stars with better than 95% success rate in

[3]On the POSS I photometric system this color range, $(O-E) \sim 0.0$ to 1.0 mag., corresponds approximately to a $(B-V) \sim 0.0$ to 0.6, and includes stars in the blue and intermediate color bins as defined in Paper I.

each field.

Table 2 lists the APS plate number for each field, the galactic coordinates for the centers of the Hydra fields, the number of fibers dedicated to stars and to blank sky, the exposure times, and which night each field was observed. For stars between 16-18th magnitude, long integrations were needed, and we used 3–4 exposures for an average of 40 minutes each. We also took a projector flat or quartz flat, and a comparison spectrum for each fiber configuration. At CTIO a projector flat and comparison spectra were taken after each exposure of the target stellar field. Because each fiber has a slightly different response depending on its location, the projector flats are used to remove any signature from the fiber itself. At KPNO, projector flats and comparison spectra were taken before a set of exposures on the initial field and at the end of the exposures on the final field. WIYN-HYDRA has a slower fiber positioner and these procedures maximized observation time. Comparison spectra were obtained and used to dispersion correct the spectra. We used the He-Ne-Ar lamp at CTIO, and the Cu-Ar lamp at KPNO. Spectra of the standards stars were observed throughout the night in the same manner using a single fiber manually positioned at the center of the field. Some stars observed on the first run, CTIO 1999, were repeated on the second run, CTIO 2000, as a further quality check. Field P566 was observed on all three runs to compare results between KPNO and CTIO.

3. Data Reduction and Velocity Measurement

HYDRA has its own software reduction task DOHYDRA within the larger Image Reduction and Analysis Facility software package (IRAF[4]). DOHYDRA is a specialized

[4]IRAF is written and supported by the IRAF programming group at the National Optical Astronomy Observatories (NOAO) in Tucson, Arizona. NOAO is operated by the Associa-

package with multiple tasks for scattered light subtraction, flat fielding, fiber throughput correction, wavelength calibration, extraction, and sky subtraction. There is a degree of automation and built-in record keeping that is necessary for the volume of data generated by this instrument. The task CCDPROC was used to correct each image for the overscan and bias. Each individual exposure was processed with DOHYDRA using the projector flats for the flat field, the comparison spectra for the dispersion correction, and a simple text table generated by the instrument to identify the apertures used. DOHYDRA first identifies the apertures, then flat fields the images by extracting and averaging the flat field spectra over all fibers. Interactively, the average flat field is fit by a high order function, spline3 order 100, that normalizes the individual flat field spectra. The spectra were then dispersion corrected after identifying lines in the comparison spectra. The three 40 minute exposures were co-added and sky subtracted, and any remaining cosmic rays or bad pixels previously not eliminated were edited out. The spectra were not continuum subtracted as this made no difference for measuring the Doppler velocities.

Nearly 1000 spectra were reduced using the above techniques. Of these 1000 spectra about 10% were not used most often because the object was fainter than 17.5 magnitude, which turned out to be the practical limit for adequate S/N for line identification and the velocity measurements. The radial velocities were measured with the IRAF task RVIDLINES. As a baseline, we manually identified 2 to 3 spectral lines and then relied on RVIDLINES to automatically identify the remaining lines from a list we created including the Balmer series, the Ca II H and K lines, and strong metallic lines found in A-G-type dwarf stars. We selected lines that could be clearly distinguished from the noise. Misidentified lines were rejected based on large velocity residuals. For the majority of the

---

tion of Universities for Research in Astronomy (AURA), Inc. under cooperative agreement with the National Science Foundation

stars the velocity error is better than $\sigma_{helio} \sim 10$ km s^{-1}. Each night, standard stars were observed and reduced following the same procedures. Table 3 shows the measured radial velocities of the standards and their errors compared with their known velocities. The velocities are consistent for all the nights and agree well with the published values. In addition, we independently compared the velocities for stars observed on multiple observing runs. Minor differences exist but were within the errors expected for measurements at this resolution. The duplicate observations were combined by taking the weighted average radial velocity for each star. Accounting for duplicates we have radial velocities for 741 stars, 418 stars in quadrant I and 323 stars in quadrant IV. The heliocentric velocities are given in Table 4.

4. Velocities, Spectral Classification and Metallicities

In this section we review the measured velocities corrected to the Local Standard of Rest (LSR) and the corresponding angular rotation rate (ω) in the two quadrants, compare the stars' kinematics with their spectral types and metallicities, and discuss the kinematics of the three primary population groups in the two quadrants.

4.1. The Kinematics

In Figure 2, we show the normalized histograms of the measured velocities for the quadrant I and IV stars corrected to the LSR using the solar motion values from Hipparcos data reported in Ibata *et al.* (1997). Both quadrants show a very broad range in velocities with high velocity tails to negative velocities in quadrant I and to positive velocities in quadrant IV as we would expect, but surprisingly both show net negative velocities. After removing the obviously high velocity Population II stars with V_{LSR} greater than $\pm$ 200 km

s^{-1}, the mean LSR–corrected velocities are -19.3 ± 3.2 km s^{-1} and -15.3 ± 4.0 km s^{-1} for quadrants I and IV, respectively with standard deviations (σ) or dispersions of 65.3 km s^{-1} and 68.8 km s^{-1}, respectively. If we assume a uniform, axisymmetric thick disk, that is rotating with a circular velocity comparable to the thin disk, an observer at the LSR would expect to measure stars with positive LSR velocities in quadrant I, as these stars are moving away from us, and negative velocities in quadrant IV since the stars would be approaching. The velocities should be comparable for stars at similar distances and symmetric directions but of opposite sign. However, the thick disk is known to rotate slower or lag the thin disk by 30 – 50 km s^{-1}. Thus, the observed LSR velocities for the thick disk would be expected to show a relative net shift with respect to the disk velocities in both quadrants, to more negative velocities in quadrant I and to more positive velocities in quadrant IV. Of course the velocity distributions in Figure 2 represent a mixture of disk, thick disk and halo stars, but the much greater shift with respect to the expected disk velocities of ≈ 10 to 25 km s^{-1} in quadrant I, shows a clear asymmetry between the stars in the two quadrants and suggests the presence of a population of stars with different kinematics and greater net "lag" in quadrant I compared to quadrant IV.

To investigate this possible lag or slower rotation in quadrant I, we have also calculated the angular rate of rotation for each star, $\omega_\star$, using the standard equation,

$$V_{LSR} = (\omega_\star - \omega_\odot)\ R_\odot\ sinl\ cosb \tag{1}$$

with $R_\odot$ = 8 kpc (see Reid (1998)), $V_\odot$ = 220 km s^{-1}, and $\omega_\odot$ = 27.5 km s^{-1} kpc^{-1}.

The histograms for the angular rate of rotation in Figure 3 show a shift in the observed rotational rate and different kinematics between the stars in quadrants I and IV. In their directions, and at 1 to 2 kpc from the Sun, these stars will typically be 6.4-7.5 kpc from the Galactic Center. Using the power law fit to the rotation curve found in Brand & Blitz (1993), stars at these galactocentric distances would have an expected ω of 30 to 38 km

s^{-1} kpc^{-1}. Removing the high velocity Population II stars with V_{LSR} greater than ± 200 km s^{-1}, the mean $\omega_\star$ for quadrant IV is 33.4 ± 1.4 km s^{-1} kpc^{-1} consistent with circular rotation. However, the stars in quadrant I have a slower effective rotation, with a mean $\omega_\star$ = 21.8 ± 1.2 km s^{-1} kpc^{-1}. *The results for V_{LSR} and ω show a kinematic asymmetry between quadrants I and IV corresponding to the observed asymmetry in the star counts.* However these results alone do not allow us to distinguish between radial streaming along the major axis of a triaxial thick disk and a rotational lag due to interaction with the bar in the disk.

Furthermore, when we inspect the results for the individual fields (Table 5), we note that there is a very interesting gradient or dependence of the mean V_{LSR} values on longitude, especially in quadrant I. The mean V_{LSR} values become more negative at the greater longitudes in quadrant I and somewhat more positive in quadrant IV. This dependence may let us separate the radial and tangential components to determine if the kinematic asymmetry is due to streaming in the radial direction or a lag entirely in the direction of Galactic rotation.

In §4.4 below, we use additional information on the stars' metallicities to re-examine their kinematics as a function of stellar population and confirm that a significant fraction of the quadrant I thick disk stars are participating in a slower effective rotation .

4.2. The Spectral Types

We have also determined approximate spectral types for all of the stars for which we have a measured radial velocity. We call our types "approximate" because we did not have observed standards for each spectral subtype, and because few standards exist for the metal-weak population. Instead, we used the reference table and online spectral catalog by

Jones (1996) (ftp://ftp.noao.edu/catalogs/coudelib), plus spectra of our velocity standards in the classification process. Comparison of the spectral types for stars observed at both CTIO '99 and WIYN '00 demonstrates that our method is internally consistent. However, we note that the stars observed during the CTIO '00 run were subject to a small light leak which produced an offset in the flux level of each spectrum. This did not affect the velocity measurements which were confirmed by comparing the results for the multiply observed stars. We classified these spectra according to the same criteria as the other stars, and comparison with the types for the stars with duplicate spectra show that the spectral types are consistent; although the classifications for these stars perhaps should be considered somewhat less reliable. All of the stars with spectra with sufficient S/N for the velocity measurements and spectral classification are listed in Table 4.

Figure 4 shows a histogram of the spectral types for stars in quadrant I compared to quadrant IV. There are approximately the same relative numbers of the different spectral types in the two quadrants with slightly more early-type stars (A8-F5) classified in quadrant I than in quadrant IV. Comparing the spectral types with the LSR velocities in Figure 5, we note that more of the A8-G0 stars in quadrant I have larger, in this case, more negative, LSR velocities, suggestive of thick disk/inner halo star velocities, than observed for the same types of stars in quadrant IV.

4.3. Metallicities

We obtained metallicity estimates for our stars using the methodology and calibration of Beers *et al.* (1999), which is based on the relationship between a CaII K-line index, KP, and the $(B-V)_0$ colors. The line indices KP and HP2 were obtained using their procedures, but since we do not have measured $(B-V)_0$ colors for our program stars, we have followed the procedure described by them based on an estimate of the de-reddened

color, from the Balmer-line index, HP2. Previous experience suggests that this procedure works quite well for stars of "intermediate" color, e.g., stars with $0.40 \leq (B-V)_0 \leq 0.80$, with an estimated scatter on the order of 0.05 mags, but exhibits somewhat higher scatter for stars with colors outside this range. The great majority of our program stars fall within this optimal color range.

Using this method we estimated the metallicities for 581 of the 741 stars in Table 4. Metallicities were not measured from those spectra with the small light leak mentioned in §4.2. Some of the spectra were also too noisy to obtain a reliable measurement and are so designated in the table. The normalized histograms for the [Fe/H] values are shown in Figure 6; the mean error in the individual [Fe/H] values ($\sigma_{[Fe/H]}$) is 0.25 dex. The distribution of the metallicities confirm our selection criteria with a predominance of thick disk and halo stars in this color range. Removing the extremely metal poor stars with [Fe/H] $<$ -2.2, the stars in quadrant I have a mean [Fe/H] = -1.06 $\pm$ 0.07, and therefore appear to be slightly more metal rich than those in quadrant IV with a mean [Fe/H] = -1.27 $\pm$ 0.12. Quadrant IV's mean [Fe/H] is close what we would expect for a mixed metal-poor population. Assuming that the stars in both quadrants are a mixed population, quadrant I apparently has relatively more stars with a higher metallicity, perhaps more representative of the thick disk population which has a mean [Fe/H] of $\approx$ -0.7. This is consistent with the excess of presumed thick disk stars (Paper I) in the quadrant I fields yielding a slightly higher metallicity.

4.4. Population Separation and the Kinematics

With this additional metallicity information, we use [Fe/H] and V_{LSR} to separate our sample into the three primary population groups and repeat our calculations of the mean V_{LSR}, and ω. As in §4.1 and §4.3 we initially remove the extreme high

velocity stars with $|V_{LSR}| \geq 200$ km s^{-1} and define the three groups according to metallicity; disk: $-0.3 \leq [Fe/H] \leq 0.30$, thick disk: $-1.2 \leq [Fe/H] \leq -0.30$ and halo: $-2.2 \leq [Fe/H] \leq -1.2$. Admittedly, given the uncertainties with our method for determining the metallicities (due primarily to the need for estimated colors), the errors in the individual [Fe/H] values, plus the natural spread and overlap in [Fe/H] for these three groups, we do not expect a clean separation. There is undoubtedly some contamination and overlap, especially between the disk and thick disk stars given our criteria. For that we reason we have used the V_{LSR} to further refine the separation. For example, a star with an [Fe/H] indicative of the disk or thick disk but with a $|V_{LSR}| \geq 150$ km s^{-1}, was reassigned to the halo population. Figures 7 and 8 show the resulting histograms for V_{LSR} and ω, respectively for the halo, thick disk and disk populations in quadrants I and IV. The mean values with their errors and standard deviations are given in Table 6.

The results for the presumed halo population are much as we would expect for a population with a high velocity dispersion with respect to the LSR. With the large dispersion in their velocities, the results for the halo population in the two quadrants do not appear to be significantly different. The quadrant I halo stars, however, do have a slightly lower mean rotational rate than for those in quadrant IV.

The differences in the mean velocities and rotation rates between the two quadrants for the thick disk and disk stars confirm our previous conclusion that a significant population of quadrant I stars are rotating slower than those in quadrant IV. Recall that the expected V_{LSR} velocities are positive and negative in quadrants I and IV, respectively, and at the distances and directions of these stars should be on the order of 10 to 25 km s^{-1}. The mean V_{LSR} values for the presumed disk and thick disk stars in quadrant IV are consistent with this expectation, but the thick disk stars do not show a significant positive shift in V_{LSR} or the slower effective rotation expected for this population. In quadrant I the shift to

more negative velocities and the rotational lag is quite apparent confirming the kinematic asymmetry affecting the thick disk stars, and to some extent the disk stars, between quadrants I and IV. We also note that the velocity dispersions for the thick disk stars in both quadrants and for the disk stars in quadrant I are noticeably higher than the nominal dispersions for the thick disk ($\approx$ 45 km s^{-1}) and for main sequence disk G stars ($\approx$ 30 km s^{-1}) which may be due to a mixture from other more high velocity populations in each case.

In §4.1, we commented on the evidence for a gradient in the mean V_{LSR} velocities with Galactic longitude (see Table 4). Using the additional information from the metallicities, we have investigated the results for V_{LSR} and ω as a function of population type in the different fields; summarized in Table 7. The thick disk stars, and to a somewhat lesser extent, the halo stars in quadrant I[5], show a dependence of their mean V_{LSR} values on longitude, while the quadrant IV stars do not show a similar dependence. The observed V_{LSR} is a combination of the stars' motions in the radial(v_r), tangential(v_ϕ), and vertical(v_z) directions (see eqn. 2) and the contribution of each to the total velocity will depend on the star's direction and distance . For example, looking toward the Galactic center, P566 and P505 ($l \approx 20°$), v_r will be the primary component, while towards l of 40° to 50° the radial and tangential contributions should be more nearly equal. Assuming that we have a uniform population of stars in these different fields with a common or shared motion, the observed dependence on longitude for the quadrant I stars should allow us to estimate the three components and determine if the quadrant I thick disk kinematics are due primarily to radial streaming or rotational lag. We have used the method of least squares applied to

$$V_{LSR} = [v_r cos\theta + (\frac{v_\phi}{R_*} - \frac{V_\odot}{R_\odot})sin\theta]cosb + v_z sinb \qquad (2)$$

where θ is the angle between the line of sight from the Sun to the star and the Galactic

[5]The disk stars are not included because there are too few in the individual fields to yield meaningful results

Center to the star, $sin\theta = R_{\odot}\mathrm{sin}l/R_{*}$, and R_{*} is the distance of the star from the Galactic Center. Assuming the stars are 1 and 2 kpc from the Sun, we solved for v_r, v_ϕ and v_z. The results are summarized in Table 8. Not surprisingly, the uncertainty in the solutions is large given the small number of stars and the intrinsic dispersions of the thick disk stars in these three directions. Nevertheless, the three parameter solution for the quadrant I stars, shows that the slower effective rotation for these stars is due to slower motion in the direction of Galactic rotation (v_ϕ) with a lag of $\sim$ 80 km s^{-1} with respect to circular rotation in the disk, and slower than the 40 – 50 km s^{-1} normally assumed for the thick disk. The radial component shows a net motion toward the Galactic Center, but it is small and probably not significant. We repeated the same solutions for the quadrant IV stars. Although there are only 55 stars in this set, the results are distinctly different than those for quadrant I. The results for v_z are sufficiently anomalous implying a large motion toward the plane and with a large error, that it is probably meaningless. We therefore repeated the solutions for both quadrants with only two parameters, setting $v_z = 0$. These solutions for quadrant IV for the two assumed distances from the Sun, yielded more uniform results with smaller errors, and show only a small rotational lag and a marginal radial outflow which is probably not significant. Interestingly, the quadrant I solutions for v_r and v_ϕ are compatible with the three parameter results with smaller errors. We conclude that the quadrant I thick disk stars have a lag of 80 – 90 km s^{-1} in the direction of Galactic rotation while a similar population in quadrant IV has a probable lag of only $\sim$ 20 km s^{-1}, confirming the kinematic asymmetry between the two directions.

5. Discussion – Possible Causes of the Asymmetry

In Paper I, we considered three possible explanations for the observed asymmetry in the stars counts, a fossil remnant from an ancient merger, a triaxial thick disk, and an

interaction with the bar in the old or thin disk in quadrant I, and concluded that either the triaxial thick disk or a bar/thick disk interaction could best explain the excess in the star counts, but that the merger remnant was less likely. Hernquist & Weinberg (1992) and Debattista & Sellwood (1998) showed that a rotating bar in the disk could induce a gravitational "wake" that would trap and pile up stars behind it and these stars may thus show a measurable lag in their rotational velocities. Likewise a triaxial thick disk could also yield different effective rotation rates because of non-circular streaming motions along the major axis.

Numerical simulations suggest that triaxial dark halos are a natural consequence of Cold Dark Matter scenarios (Dubinski & Carlberg 1991). Based on studies of rotating triaxial spheroids Blitz & Spergel (1991) suggested that there may be both a rounder outer halo and a triaxial (flattened) inner halo. This model is supported by observations that show both a round outer halo (Hartwick (1987),Chiba & Beers (2000)) and evidence for a large flattened distribution in the inner halo (Wyse & Gilmore (1989), Larsen & Humphreys (1994), Chiba & Beers (2000)). Curir & Mazzei (1999) also find a high probability that a rotationally supported disk and a non-axisymmetric halo can trigger instabilities leading to the formation of a long-lived bar. Their simulations also suggest that these instabilities are similar in character to spiral-density waves, and can affect stars at higher Galactic latitudes in a similar way.

For some time now, there has been substantial evidence for a bar within the bulge of the Milky Way, but numerous more recent studies in the Galactic plane ($b \pm 3°$) (Blitz & Spergel 1991; Weinberg 1992; Lopez-Correidoira et al. 1999; Feast and Whitelock 2000; Hammersley et al. 2000) have revealed the presence of a stellar bar extending beyond the bulge with a 3-5 kpc radius. Weinberg (1994) demonstrated that a structure with a rotating pattern speed in a disk system, assuming nearly circular orbits, generates three resonances:

the inner Linblad (ILR), the outer Linblad (OLR) and another at the corotation location (CR), which can lead to significant kinematic signatures in the line-of-sight velocities and velocity distributions. In his model, a triaxial rotating spheroid will produce an increased velocity dispersion near the OLR at approximately 4-5 kpc from the galactic center. The high overall velocity dispersion measured for the stars in our study may be explained by the OLR of a triaxial thick disk or inner halo. However, it is just as likely that losses in angular momentum of a moderate stellar bar may reduce the bar's pattern speed and inflate the velocity dispersions in the thick disk. Weinberg (1994) finds that the latter explanation supports his predictions of a stellar bar at 5 kpc with a position angle of 36°, see Figure 3 in Weinberg (1992)

The effect of a bar on its parent galaxy is dependent on the amount and distribution of dark matter in the galaxy. It has not yet been determined if a stellar bar is created by the interaction between a thin disk and an outer (potentially dark matter) halo, which then creates an asymmetric, triaxial thick disk/inner halo, or whether, alternatively, the presence of a triaxial thick disk/inner halo contributes to bar formation. In either case, the kinematics would be similar and the bar and major axis of the thick disk would be nearly aligned. If the leading edge of the triaxial thick disk is in quadrant I, as implied by the star count excess, the differences between the rotational kinematics would lead to a more negative lag in the velocities in quadrant I as would a gravitational interaction with the disk bar also in quadrant I. Thus our results for a kinematic asymmetry between quadrants I and IV and slower effective rotation in quadrant I could be due to either cause.

The mean V_{LSR} velocities and rotation rates (ω) for the separate fields in quadrant I also show a dependence on Galactic longitude for the thick stars not shown by the stars in quadrant IV. Least squares solutions for the three velocity components of the V_{LSR} show that the thick disk stars in quadrant I have a major lag in their velocities in the direction of

Galactic rotation much slower than for the quadrant IV stars and slower than the nominal thick disk lag, with no significant radial component. This result supports a gravitational interaction with the bar as the more probable explanation for the observed asymmetries. This does not necessarily mean that the thick disk is not triaxial. As discussed above, bar/thick disk interactions may be independent of a triaxial thick disk, or it might be the case that triaxial thick disks are a dynamical result of bar formation or vice versa and the two may be nearly aligned.

To further investigate the possibility that the asymmetry feature is a consequence of a gravitational wake induced by a stellar bar, Debattista and Sellwood (private communication) have added a thick disk component to their models, and followed the evolution as a bar forms and rotates in the thin disk. Their preliminary results show that the non-axisymmetric response in the thick disk induced by the interaction with the stellar bar can give better agreement with the observed asymmetries in the star counts and kinematics. These models and a detailed comparison with the observations will be presented in a later paper (Debattista & Sellwood 2003).

In Paper I, we found a significant excess of thick disk/inner halo stars in quadrant I above and below the galactic plane extending from $l \sim 20^\circ - 55^\circ$ and $|b|$ $20^\circ - 45^\circ$ covering more than 600 ($\times$ 2) square degrees. Doppler velocities, spectral types and metallicities reported here from spectra of 741 stars in quadrants I and IV reveal a kinematic asymmetry as well which shows most strongly among the thick disk stars. The stars in quadrant I have a negative mean LSR velocity with a significant net shift in the expected LSR velocity, a slower effective rotation rate, and a slightly higher mean metallicity than the stars in quadrant IV. *We also demonstrate that the quadrant I thick disk stars have a significant lag in their velocities in the direction of galactic rotation, much slower than found for the quadrant IV stars and slower than normally assumed.* These results tend to support a

gravitational interaction between the thick disk stars and the rotating stellar bar in the disk as the best explanation for the asymmetry in the star counts and the kinematics. Combined with the evidence reported by Larsen & Humphreys (2003) that some parameters such as the scale height and the normalization may vary with direction, the characteristics of the thick disk population, including its kinematics, may depend on where one is looking.

After this paper was submitted, the discovery of the Canis Major merger remnant was announced by Martin *et al.* (2004). Their detection of an extensive remnant relatively nearby close to the Galactic plane, suggests that such events may be the origin of the thick disk. In Paper I we rejected a merger remnant as an explanation for the star count excess in quadrant I for several reasons, including the shape and extent of the asymmetry region on the sky, its presence above and below the plane, and a comparison with the debris field of the Sagittarius dwarf merger. However, the debris left by Canis Major or other mergers could contribute to our observed asymmetry in the star counts and kinematics and to the varying characteristics of the thick disk with direction (Larsen & Humphreys 2003). The region of our observed asymmetry is not reproduced in the simulations for Canis Major (Martin *et al.* 2004), although this does not necessarily eliminate the role of this or another merger. Indeed the star count excess and much slower rate of rotation for the thick disk stars in the asymmetry feature could be due to interaction of a merger remnant with the bar in the disk. An important question to be decided with additional observations and modelling is whether the thick disk/inner halo populations sampled in quadrants I and IV are a single population with asymmetric spatial and kinematic properties or are two different populations.

Future work will include additional velocity measurements at higher longitudes and in fields below the Galactic plane plus the addition of proper motions from the APS Catalog and other all–sky surveys. These additional observations will help to further clarify the

origin of the asymmetry.

We are grateful to the support staff at both CTIO and KPNO for their excellent support with the HYDRA spectrograph and we especially want to thank Nick Suntzeff and Riccardo Venegas at CTIO. We are pleased to acknowledge very useful commuications with Jerry Sellwood and Victor Debattista. We also thank Kris Davidson for his programming assistance with the least squares solutions. The APS project has been supported by the NSF, NASA and the University of Minnesota. This work was supported in part by NASA's Applied Information Systems Research Program (NAG 5-9407). T.C.B. acknowledges partial support for this work from NSF grants AST 00-98508 and AST 00-98549, awarded to Michigan State University.

REFERENCES

Blitz, L. & Spergel, D.N., 1991, ApJ, 379, 631.

Brand, J. & Blitz, L., 1993, A&A, 275, 67B.

Beers, T.C., Rossi, S., Norris, J.E., Ryan, S.G., & Shefler, T. 1999, AJ,117, 981

Chiba, M. & Beers, T. C. 2000, AJ, 119, 2843.

Curir, A. & Mazzei, P., 1999, A&A, 352, 103.

Debattista, V. P. & Sellwood, J. A., 1998, ApJ, 493, L5.

Debattista, V. P. & Sellwood, J. A., 2000, ApJ, 543, 704.

Debattista, V.P. and Sellwood, J.A., 2003, in preparation.

Dubinski, J. & Carlberg, R.G., 1991, 378, 496.

Feast, M.W. & Whitelock, P.A., 2000, MNRAS, 317, 460.

Hammersley, P.L., Garzon, F., Mahoney, T.J., Lopez-Corredoira, M. & Torres, M.A., 2000, MNRAS, 317, 45.

Hartwick, F.D.A., The Galaxy: Proceedings of the NATO Advanced Study Institute, (Dordrecht: D. Reidel Publishing Co.), 1987, p. 281-290.

Hernquist, L, & Weinberg, M. D., 1992, ApJ, 400, 80

Ibata, R.A., Wyse, R.F., Gilmore, G., Irwin, M.J. & Suntzeff, N. B., 1997, AJ, 113, 634.

Jones, L.A., 1996, Ph.D. Thesis, University of North Carolina at Chapel Hill.

Larsen, J.A. & Humphreys, R.M., 1994, ApJ, 436, L149.

Larsen, J.A. & Humphreys, R.M., 1996, ApJ, 468, L99.

Larsen, J.A. & Humphreys, R.M., 2003, AJ, 125, 1958.

Lopez-Corredoira, M., Garzon, F., Beckman, J.E., Mahoney, T.J., Hammersley, P.L., & Calbet, X., 1999, AJ, 118, 381.

Martin, N. F., Ibata, R. A., M. Bellazini, M., Irwin, M. J., Lewis, G. F., & Dehnen, W., 2004, MNRAS, in press

Parker, J.E., Humphreys, R.M., & Larsen, J.A. 2003, AJ, 126, 1346.

Reid, I.N., 1998, AJ, 115, 4.

Weinberg, M.D., 1992, ApJ, 384, 81.

Weinberg, M.D., 1994, ApJ, 4, 597.

Wyse, R. F. G. & Gilmore, G. 1989, *Comments on Astrophysics*, 13, 135.

Fig. 1.— A map of the selected fields observed at CTIO and KPNO. The light gray identifies observations made on the Blanco 4m at CTIO in 1999, dark gray for the 2000 observations and black indicates those fields observed with the WIYN 3.5m at KPNO in 2000.

Fig. 2.— Normalized histograms of the LSR velocities for quadrants I(a) and IV(b).

Fig. 3.— Normalized histograms of the angular rotation rates between quadrants I(a) and IV(b).

Fig. 4.— A normalized histogram of the spectral types for quadrants I and IV.

Fig. 5.— LSR velocities versus spectral types for quadrant I(a) and IV(b).

Fig. 6.— Normalized histograms of metallicities for quadrants I and IV. a) Q1 has an average metallicity [Fe/H] = -1.06 $\pm$ 0.07 whereas b) quadrant IV has a mean [Fe/H] = -1.27 $\pm$ 0.12.

Fig. 7.— The distribution of V_{LSR} with population type in quadrants I and IV; a-b) halo c-d) thick disk e-f) disk.

Fig. 8.— The distribution of ω with population type in quadrants I and IV; a-b) halo c-d) thick disk e-f) disk.

Table 1. HYDRA: Instrument Specifics

Parameter	Units	Observing Runs		
		CTIO 4-m	CTIO 4-m	KPNO/WIYN 3.5-m
		Apr. 15-18, 1999	May 27-30, 2000	June 2-5, 2000
CCD		Loral 3K-1	Loral 3K-1	T2KC
Grating		KPGL-1	KPGL-1	KPC007
Grating Tilt	[°]	7.923	7.923	23.047
Gain	[e^-/ADU]	1.99	1.99	1.7
Lines/mm		632	632	632
Read Noise	[e^-/rms]	7.8	7.8	4.3
Binning		1×2	1×2	1×1
Central λ	[Å]	4167	4167	4270
Dispersion	[Å/pix]	1.0378	1.0378	0.986
Fibers		Large	Large	Blue
Usable Fibers		70/138	70/138	98/100
Quartz		He-Ne-Ar	He-Ne-Ar	Cu-Ar

Table 2. Observations

Field	l[°]	b [°]	Fibers		Exp Time	Nights
			Stars	Sky	[min]	Observed
CTIO 1999						
P913	320.0	30.0	54	4	40 × 4	April 15
P566	20.0	32.0	50	5	40 × 3, 60	April 15,17
P858	329.0	32.0	54	5	40 × 4	April 16
P802	339.5	33.0	55	5	40 × 4	April 17
P741	339.0	41.0	53	5	40 × 4	April 17
P799	320.0	41.0	52	4	40 × 3	April 18
P505	21.0	42.5	50	5	40 × 3	April 18
CTIO 2000						
P913	320.0	30.0	56	5	40 × 3	May 27
P802	339.5	33.0	49	4	40 × 2	May 27
P566	20.0	32.0	57	3	40, 40, 40	May 27,28,29
P799	320.0	41.0	52	5	40 × 3	May 28
P858	329.0	32.0	50	5	40 × 3, 40	May 28,29
P855	309.0	37.0	55	4	40 × 3	May 29
P741	339.0	41.0	56	5	40 × 3	May 29
WIYN 2000						
P387	40.0	41.0	80	5	40 × 3	June 2
P448	40.0	30.0	77	5	40 × 3	June 2
P505	21.0	42.5	81	5	40 × 3	June 3
P566	20.0	32.0	79	5	40 × 3	June 3
P507	31.0	32.0	83	5	40 × 3	June 4
P332	51.0	37.0	85	5	40 × 3	June 4
P566-1	20.0	32.0	77	5	40 × 3	June 5

Table 3. Radial Velocity Standards

Star	V_r [a] [km s^{-1}]	Spectral Type [a]	Measured Radial Velocities [km s^{-1}]			
			night 1	night 2	night 3	night4
CTIO 1999			April 15	April 16	April 17	April 18
HD 136202	53.5 ± 0.2	F8 IV-V	54.0 ± 4.0	52.7 ± 3.4	53.2 ± 4.3	53.3 ± 4.4
HD 114762	49.9 ± 0.5	dF7/F9 V	-	47.5 ± 5.5	49.6 ± 6.6	49.5 ± 2.0
HD 86986	8.7	A1 V	8.3 ± 3.0	8.9 ± 2.6	8.9 ± 3.0	8.7 ± 2.2
HD 89449	6.5 ± 0.5	F6 IV	-	6.7 ± 1.9	6.8 ± 2.5	6.3 ± 2.4
CTIO 2000			May 26	May 27	May 28	May 29
HD 180134	-23.5	F7 V	-	-23.7 ± 5.9	-22.9 ± 4.7	-23.2 ± 4.2
HD 188642	-30.8	F4 V	-	-31.6 ± 3.8	-30.2 ± 5.9	-30.7 ± 2.4
HD 203638	21.9	KO III	-	21.3 ± 4.0	19.7 ± 3.1	20.8 ± 5.4
WIYN 2000			June 2	June 3	June 4	June 5
HD 136202	53.5 ± 0.2	F8 IV-V	52.5 ± 4.9	53.3 ± 4.9	53.2 ± 4.0	-
HD 114762	49.9 ± 0.5	dF7/F9 V	51.0 ± 4.9	50.8 ± 6	51.0 ± 5.5	51.9 ± 4.8
HD 161817	-362.8	sdA2	-367.4 ± 4.8	-364.0 ± 3.8	-364.5 ± 1.7	-362.3 ± 6.5
BD 28 3402	-36.6 ± 0.5	F5 V	-36.7 ± 3.4	-36.1 ± 3.7	-37.8 ± 2.5	-37.8 ± 3.3

[a]standard values reported from SIMBAD http://simbad.u-strasbg.fr/Simbad

Table 4. Velocities, Spectral Types and Metallicities [a]

Field [b] /Obs. Run	APS Star [c] Number	O Mag	$(O-E)$	$l[^\circ]$	$b[^\circ]$	V_{helio} km s^{-1}	σ_{helio} km s^{-1}	Number Lines	$[\frac{Fe}{H}]$ [d]	$\sigma_{[\frac{Fe}{H}]}$	Spec. Type
P332/3	1931756	16.1	0.8	51.3	37.1	12.5	3.6	4	-0.71	0.15	G5-G8
	2058237	16.5	0.6	50.9	37.5	-80.3	11.5	4	0.30	0.22	GO
	2500783	16.0	0.6	50.3	36.8	-31.8	3.7	6	0.30	0.15	G5
	2199563	16.1	0.9	50.5	37.5	-108.6	11.1	6	-0.99	0.31	G5-G8
	1922793	15.9	0.7	51.1	37.4	-84.8	9.9	8	-0.46	0.35	G5-G8
	2215458	16.3	0.6	50.7	36.9	-153.4	8.8	4	-1.01	0.15	F5

[a]The complete version of this table is in the electronic edition of the Journal. The printed edition contains only a sample.

[b]1, 2, 3 refer to the three observing runs CTIO 1999, CTIO 2000, and WIYN 2000 respectively.

[c]Positions for the stars can be obtained from the Minnesota Automated Plate Scanner(MAPS) Catalog of the POSS I using either the sql-based query for individual stars (http://aps.umn.edu/catalog/sql.html) or the skybox query ((http://aps.umn.edu/catalog) for a region on the sky.

[d]Stars with spectra considered too noisy to obtain reasonable abundance estimates have a ... as their [Fe/H] value and are not used in the measurement of the mean. Stars with inferred $(B-V)_0$ colors outside the "optimum range" are labeled with a ":". Stars with a noisy spectrum, but have an abundance estimate are labeled with a "N".

Table 5. Mean LSR Velocities and Rotation Rates for Quadrant I and IV Fields

Field	*l, b*	N_{stars}	$< V_{LSR} >$ km s^{-1}	$\sigma_{V_{LSR}}$ km s^{-1}	$< \omega >$ km s^{-1}kpc^{-1}	σ_{ω} km s^{-1}kpc^{-1}
Q I		405	-19.2 ± 3.2	62.3	21.8 ± 1.2	23.2
P332	51.0, 37.0	37	-42.1 ± 8.4	51.2	19.0 ± 1.7	10.4
P387	40.0, 41.0	57	-35.0 ± 7.6	57.3	18.4 ± 2.0	14.9
P448	40.0, 30.0	60	-15.9 ± 8.1	62.8	23.9 ± 1.8	14.1
P507	31.0, 32.0	65	-20.7 ± 8.6	69.5	21.6 ± 2.5	20.0
P505	21.0, 42.5	64	-26.4 ± 8.3	66.2	14.9 ± 3.9	31.5
P566	20.0, 32.0	122	-1.0 ± 5.7	63.2	27.1 ± 2.5	27.1
Q IV		317	-15.3 ± 3.9	68.8	33.4 ± 1.4	24.2
P855	309.0, 37.0	31	14.9 ± 10.8	60.2	24.5 ± 2.2	12.2
P799	320.0, 41.0	60	-8.7 ± 8.5	66.1	29.7 ± 2.2	17.4
P913	320.0, 30.0	54	-16.1 ± 7.9	58.0	31.1 ± 1.8	13.1
P858	329.0, 32.0	43	-14.5 ± 13.1	86.3	31.7 ± 3.8	25.1
P741	339.0, 41.0	63	-33.3 ± 8.3	65.5	42.7 ± 3.9	30.7
P802	339.5, 33.0	66	-18.2 ± 8.8	71.8	35.1 ± 3.7	30.4

Table 6. Mean LSR Velocities and Rotation Rates for the Three Populations

Population	N_{stars}	$< V_{LSR} >$ km s^{-1}	$\sigma_{V_{LSR}}$ km s^{-1}	$< \omega >$ km s^{-1}kpc^{-1}	σ_ω km s^{-1}kpc^{-1}
Q I					
Disk	24	-6.9 ± 9.8	47.8	26.4 ±3.3	16.2
Thick Disk	195	-12.9 ± 4.1	57.6	24.5 ± 1.4	19.4
Halo	152	-34.4 ± 5.7	70.5	16.2 ± 2.1	25.9
Q IV					
Disk	8	-16.1 ± 12.6	35.9	30.7 ± 3.7	10.4
Thick Disk	55	-24.1 ± 8.4	62.3	36.4 ± 2.9	21.5
Halo	99	-27.8 ± 7.2	71.4	38.2 ± 2.7	27.0

Table 7. Mean LSR Velocities and Rotation Rates for the Populations in Different Fields

Field & Population	*l*, *b*	N_{stars}	$< V_{LSR} >$ km s^{-1}	$\sigma_{V_{LSR}}$ km s^{-1}	$< \omega >$ km s^{-1}kpc^{-1}	σ_ω km s^{-1}kpc^{-1}
Q I						
P332	51.0, 37.0					
Thick Disk		23	-35.6 ± 9.2	44.1	20.3 ± 1.9	9.0
Halo		6	-105.0 ± 22.4	54.9	6.2 ± 4.5	11.1
P387	40.0, 41.0					
Thick Disk		22	-22.4 ± 8.0	37.5	21.7 ± 2.1	9.7
Halo		31	-48.7 ± 10.8	60.2	14.9 ± 2.8	15.6
P448	40.0, 30.0					
Thick Disk		37	-18.7 ± 8.4	51.1	23.3 ± 1.9	11.5
Halo		15	-33.0 ± 20.0	77.5	20.0 ± 4.5	17.4
P507	31.0, 32.0					
Thick Disk		44	-14.3 ± 10.4	69.0	23.4 ± 3.0	19.8
Halo		15	-36.0 ± 20.8	80.5	17.2 ± 6.0	23.1
P505	21.0, 42.5					
Thick Disk		21	-5.6 ± 10.6	48.4	24.8 ± 5.0	23.0
Halo		38	-31.0 ± 11.3	69.5	12.8 ± 5.3	32.9
P566	20.0, 32.0					
Thick Disk		48	+5.1 ± 8.9	61.9	29.7 ± 3.8	26.6
Halo		47	-18.7 ± 9.6	66.0	19.5 ± 41.	28.4
Q IV						
P855[a]	309.0, 37.0					
P799	320.0, 41.0					
Thick Disk		9	-23.9 ± 23.6	70.7	33.7 ± 6.1	18.2
Halo		9	-11.8 ± 20.5	61.4	30.6 ± 5.3	15.8
P913	320.0, 30.0					
Thick Disk		10	-18.5 ± 16.1	50.8	31.7 ± 3.6	11.4
Halo		18	-29.5 ± 13.9	59.0	34.1 ± 3.1	13.3
P858	329.0, 32.0					
Thick Disk		6	-20.3 ± 41.9	102.6	33.3 ± 12.1	29.7
Halo		24	-8.9 ± 14.5	71.1	30.0 ± 4.2	20.6

Table 7—Continued

Field & Population	*l, b*	N_{stars}	$< V_{LSR} >$ km s^{-1}	$\sigma_{V_{LSR}}$ km s^{-1}	$< \omega >$ km s^{-1}kpc^{-1}	σ_{ω} km s^{-1}kpc^{-1}
P741	339.0, 41.0					
Thick Disk		12	-43.9 ± 12.2	42.4	47.4 ± 5.6	19.6
Halo		23	-57.9 ± 13.3	64.0	54.1 ± 6.1	29.4
P802	339.5, 33.0					
Thick Disk		18	-23.0 ± 12.2	51.6	33.9 ± 5.3	22.6
Halo		24	-21.6 ± 16.6	81.5	37.0 ± 6.9	33.9

[a]No [Fe/H] measurements for population separation.

Table 8. Results of the Solutions for the Velocity Components of the Thick Disk Motions

Quadrant	N_{stars}	Distance	v_r km s^{-1}	v_ϕ km s^{-1}	v_z km s^{-1}
Q I	195	1 kpc	-40 ± 26	146 ± 28	-23 ± 26
		2 kpc	-33 ± 23	141 ± 31	-18 ± 46
Q I	195	1 kpc	-28 ± 15	136 ± 21	...
		2 kpc	-23 ± 15	132 ± 18	...
Q IV	55	1 kpc	-38 ± 57	173 ± 42	-107 ± 87
		2 kpc	-45 ± 71	157 ± 39	-113 ± 88
Q IV	55	1 kpc	31 ± 34	207 ± 53	...
		2 kpc	26 ± 34	197 ± 47	...

This figure "JParker_fig01.jpg" is available in "jpg" format from:

http://arXiv.org/ps/astro-ph/0312017v1

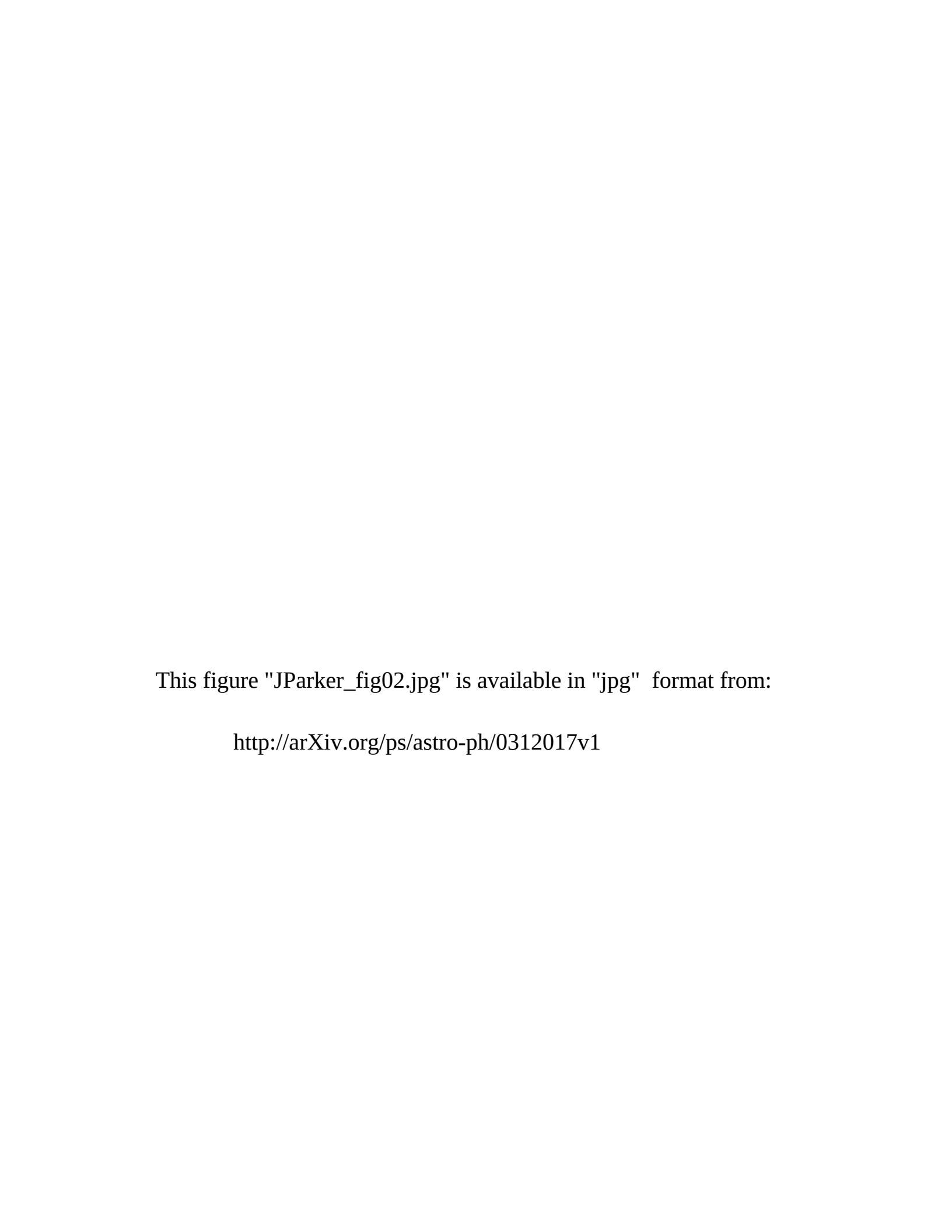
This figure "JParker_fig02.jpg" is available in "jpg" format from:
http://arXiv.org/ps/astro-ph/0312017v1

This figure "JParker_fig03.jpg" is available in "jpg" format from:

http://arXiv.org/ps/astro-ph/0312017v1

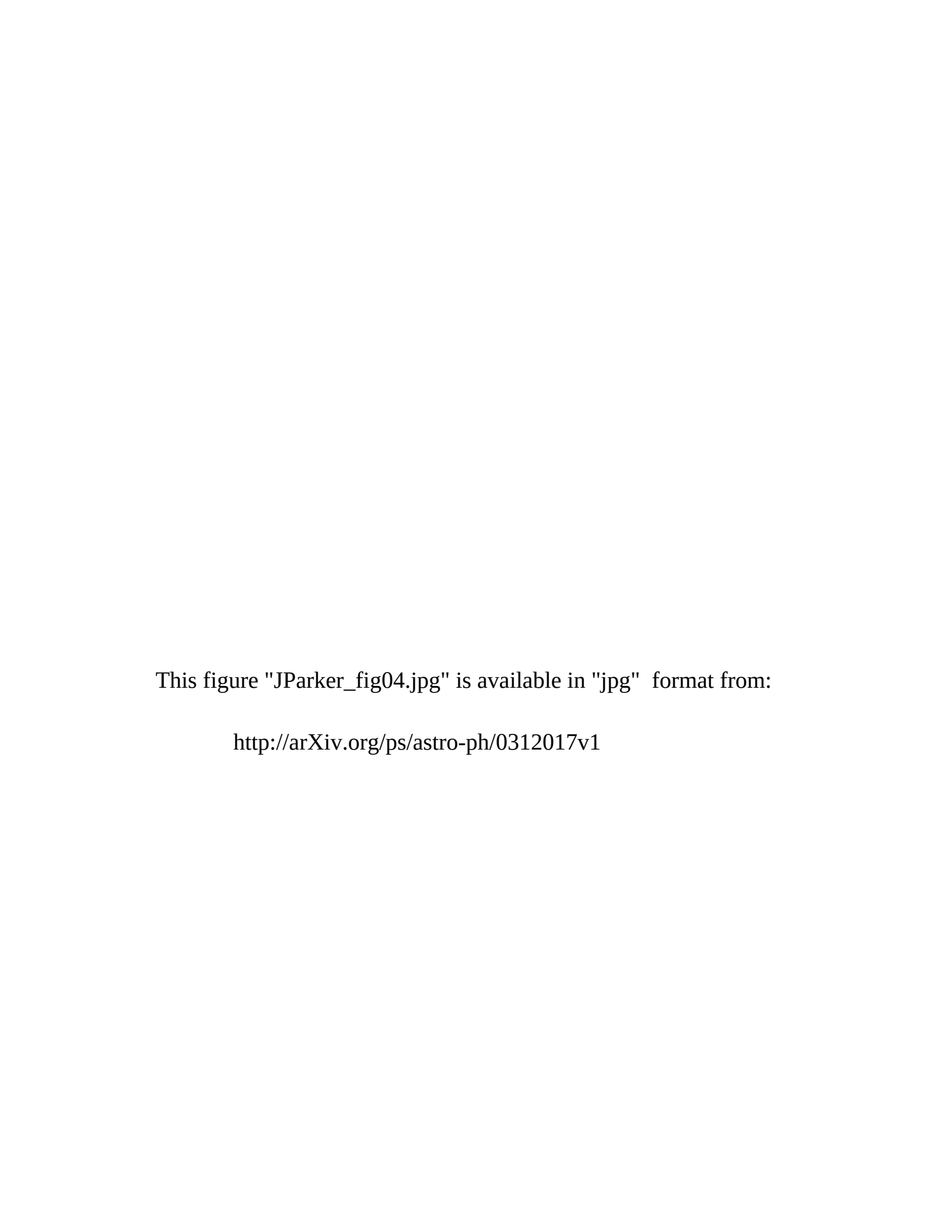
This figure "JParker_fig04.jpg" is available in "jpg" format from:
http://arXiv.org/ps/astro-ph/0312017v1

Table 4. Velocities, Spectral Types and Metallicities

Field [a] /Obs. Run	APS Star [b] Number	O Mag	$(O-E)$	$l[^\circ]$	$b[^\circ]$	V_{helio} km s^{-1}	σ_{helio} km s^{-1}	Number Lines	$[\frac{Fe}{H}]$ [c]	$\sigma_{[\frac{Fe}{H}]}$	Spec. Type
P332/3	1931756	16.1	0.8	51.3	37.1	12.5	3.6	4	-0.71	0.15	G5-G8
	2058237	16.5	0.6	50.9	37.5	-80.3	11.5	4	0.30	0.22	GO
	2500783	16.0	0.6	50.3	36.8	-31.8	3.7	6	0.30	0.15	G5
	2199563	16.1	0.9	50.5	37.5	-108.6	11.1	6	-0.99	0.31	G5-G8
	1922793	15.9	0.7	51.1	37.4	-84.8	9.9	8	-0.46	0.35	G5-G8
	2215458	16.3	0.6	50.7	36.9	-153.4	8.8	4	-1.01	0.15	F5
	1924895	17.0	0.9	51.0	37.3	-45.2	7.7	6	-0.46	0.35	GO
	2494273	16.4	1.0	50.2	37.1	-104.0	8.9	8	0.30	0.15	G8
	2057644	16.9	0.8	50.7	37.4	-19.7	4.6	8	-0.64	0.28	GO
	2071695	17.0	0.9	51.0	37.0	44.4	7.6	3	-0.42	0.35	G8
	2495225	15.9	0.7	50.1	37.0	-57.8	7.4	9	-0.30	0.29	GO
	1919857	16.9	0.5	51.0	37.5	-195.1	8.6	8	-0.47	0.17	F2-F5
	2071813	16.0	0.8	51.0	37.0	-32.6	2.9	7	-2.12	0.15	A2
	2201409	17.0	0.9	50.5	37.4	-298.0	8.2	7	-0.49	0.15	F2
	1925685	16.4	1.0	51.1	37.3	-55.6	1.7	6	-0.61	0.37	G5-G8
	2501263	16.1	0.9	50.2	36.8	-147.0	11.2	8	0.26	0.16	G2-G5
	2062883	16.2	1.0	51.0	37.3	-88.2	7.3	10	-0.44	0.27	GO-G2
	2350403	15.9	0.8	50.3	37.1	-1.5	10.6	14	-0.13	0.19	G2-G5
	2492336	16.3	0.9	50.2	37.2	-35.3	5.0	6	-0.85	0.25	G2-G5
	2342121	17.1	0.8	50.3	37.4	-66.8	4.5	4	-1.57	0.15	F5
	2057076	16.6	1.0	50.7	37.5	-104.9	5.0	9	-0.84	0.29	GO-G2
	2201010	17.2	0.8	50.6	37.4	-10.7	4.1	6	-0.30	0.31	G2-G5
	2064086	15.8	0.9	50.8	37.2	42.7	5.4	10	-0.06	0.27	GO-G2
	2205018	17.0	0.9	50.6	37.3	-124.6	6.8	7	-0.83	0.39	G5
	2057288	16.4	1.0	50.9	37.5	-17.9	3.2	6	-0.69	0.15	F8
	1923351	16.2	0.9	51.1	37.4	-72.8	2.9	4	-0.42	0.35	G5-G8
	2494781	16.5	0.9	50.2	37.1	-38.8	7.8	7	-0.30	0.33	G2-G5
	2346573	16.4	0.9	50.4	37.2	-72.2	4.8	6	-0.08	0.25	G2-G5
	2346309	16.0	0.9	50.4	37.3	-24.4	4.5	8	-0.88	0.34	G2-G5
	2210330	17.0	0.7	50.6	37.1	23.1	10.5	4	-0.44	0.27	GO
	1925176	15.9	1.0	51.2	37.3	-66.4	5.5	7	-0.60	0.36	G2-G5

Table 4—Continued

Field [a] /Obs. Run	APS Star [b] Number	O Mag	$(O-E)$	$l[^\circ]$	$b[^\circ]$	V_{helio} km s^{-1}	σ_{helio} km s^{-1}	Number Lines	$[\frac{Fe}{H}]$ [c]	$\sigma_{[\frac{Fe}{H}]}$	Spec. Type
	2056357	16.9	0.8	50.8	37.5	-49.8	7.7	11	-0.44	0.27	GO
	2349151	15.8	0.8	50.4	37.1	-110.8	5.0	7	-0.50	0.31	G2
	2345955	16.7	1.0	50.3	37.3	-11.2	2.6	5	-0.17	0.25	GO-G2
	2205036	15.9	0.9	50.6	37.3	-51.2	7.9	6	-0.85	0.25	GO
	2059092	17.4	0.9	50.9	37.4	-132.2	6.9	5	-0.50	0.31	F5
	2342112	16.8	0.8	50.4	37.4	-68.0	7.8	4	0.19	0.24	F2
	2496394	16.6	0.7	50.1	37.0	-282.5	14.6	7	...	... /	F2
P387/3	3416745	17.3	1.0	39.5	41.5	-78.1	8.1	5	-2.58	0.21	GO
	3237441	16.7	0.5	39.9	41.4	-132.9	12.0	4	-1.36	0.15	F5
	3614626	16.0	1.1	39.4	40.9	111.5	9.2	6	-2.40	0.16	F8
	3237768	16.7	1.0	39.7	41.3	-80.0	3.8	9	-1.72	0.28	G5
	3426148	15.9	0.8	39.7	41.2	-36.7	3.2	9	-0.84	0.21	GO
	3434677	17.1	0.7	39.6	40.9	-106.3	1.6	4	-2.60	0.19	F2
	3431457	16.5	0.9	39.7	41.0	-301.5	6.4	7	-2.22	0.15	F6
	2866176	17.0	0.8	40.2	41.4	-37.7	6.5	5	-1.15	0.15	F8
	3056508	16.8	0.8	40.2	41.4	46.8	1.2	3	-1.28	0.15	GO
	3605165	15.9	0.7	39.2	41.2	-281.4	8.5	7	-2.32	0.22	F2
	3608432	17.5	1.0	39.3	41.0	-38.0	7.0	7	-1.00	0.16	G8
	3415957	17.1	0.8	39.5	41.5	-220.7	6.6	7	-1.66	0.27	G2
	3426394	16.8	0.9	39.5	41.1	-166.6	13.8	6	-1.98	0.15	F2
	3231576	17.0	0.8	39.7	41.6	15.4	4.8	4	-2.37	0.15	F6
	3066736	17.5	0.8	40.3	41.1	-74.9	5.8	6	-1.93	0.23	G5
	3074101	16.4	0.8	40.2	40.8	77.5	5.5	6	-2.08	0.34	G8
	3070330	16.3	0.6	40.3	40.9	-53.6	2.6	9	-0.85	0.25	GO
	3254100	16.4	0.9	40.1	40.8	-51.6	2.1	5	-1.50	0.24	GO
	2877378	16.6	0.8	40.4	41.1	-9.4	1.7	4	-1.52	0.27	GO
	3254238	17.3	0.9	40.1	40.8	-148.3	4.6	5	-1.32	0.18	F8
	3253481	15.8	0.9	40.1	40.9	-56.7	4.2	7	-1.07	0.35	GO
	3059105	16.3	0.7	40.1	41.3	-120.5	9.1	3	-1.35	0.22	GO
	3600765	16.0	0.8	39.3	41.3	-33.2	4.4	5	-1.57	0.15	F2
	3052005	16.8	0.8	40.1	41.6	-46.9	0.8	5	-1.18	0.30	G2

Table 4—Continued

Field [a] /Obs. Run	APS Star [b] Number	O Mag	$(O-E)$	$l[^\circ]$	$b[^\circ]$	V_{helio} km s^{-1}	σ_{helio} km s^{-1}	Number Lines	$[\frac{Fe}{H}]$ [c]	$\sigma_{[\frac{Fe}{H}]}$	Spec. Type
	3234973	17.2	0.8	39.7	41.5	-72.5	4.6	7	-0.88	0.34	G8
	3604210	16.6	1.1	39.3	41.2	-52.8	6.4	8	-1.03	0.28	G2
	3239898	16.9	1.1	39.9	41.3	-78.7	4.3	9	-1.33	0.35	G8
	3423906	16.7	0.9	39.5	41.2	-54.4	4.2	5	-0.65	0.25	G2
	3417048	16.2	1.0	39.4	41.5	38.1	3.1	8	-1.03	0.28	G2
	2867989	17.4	0.9	40.4	41.4	34.4	1.3	5	-0.88	0.36	G5-G8
	3066763	16.6	1.0	40.2	41.0	-99.1	11.9	7	-1.11	0.15	GO
	3232899	17.3	0.3	39.6	41.5	-228.5	4.5	5	-2.19	0.15	F2
	2868159	16.5	1.0	40.3	41.4	18.6	1.5	6	-1.20	0.28	GO
	3433356	16.6	1.0	39.6	40.9	-16.4	3.5	7	-1.34	0.30	G8
	2868793	17.3	0.7	40.4	41.4	-105.1	10.9	6	-1.58	0.15	F5
	3437117	16.8	1.0	39.6	40.8	-41.2	4.2	6	-1.18	0.30	G2
	2863451	17.1	0.9	40.2	41.5	-51.2	2.4	6	-0.64	0.28	G2
	3069041	16.8	1.0	40.3	41.0	47.5	5.0	8	-1.03	0.28	GO
	3232741	15.8	0.9	39.8	41.6	-29.9	4.4	8	-1.67	0.33	G8
	3230124	16.6	0.5	39.6	41.6	-62.3	6.9	6	-1.47	0.21	F8
	2871291	15.8	0.9	40.3	41.3	-81.4	1.7	5	-1.18	0.30	G2
	3441984	16.1	1.0	39.9	40.7	-98.9	4.0	8	-1.72	0.28	G8
	3234863	16.2	0.8	39.7	41.4	-67.1	3.8	8	-1.02	0.21	F8
	3056057	17.1	1.0	40.0	41.4	-38.7	5.3	5	-1.16	0.41	G8
	2865684	17.2	0.7	40.2	41.5	-24.4	4.7	6	-1.80	0.32	G8
	3250808	16.3	1.1	40.0	40.9	0.3	3.4	5	-1.18	0.30	G5
	3427252	17.7	0.9	39.6	41.1	-62.2	2.2	5	-1.94	0.33	G8
	3256718	16.3	1.1	39.9	40.7	-125.6	6.5	7	-1.51	0.29	G5
	3417845	16.1	0.9	39.4	41.4	-15.5	3.7	5	-0.69	0.15	GO
	3418359	17.6	0.7	39.4	41.4	-78.0	3.4	6	-1.07	0.35	G8
	2868126	16.5	0.6	40.3	41.4	-33.6	2.9	8	-1.18	0.30	G2
	3048658	16.9	0.7	39.9	41.6	-110.0	8.4	8	-1.86	0.15	GO
	3601819	17.2	1.0	39.2	41.3	-200.5	6.7	5	-1.03	0.15	F4
	3067595	17.0	0.6	40.2	41.0	-51.9	7.8	5	-1.47	0.21	G2
	3238735	16.2	1.1	39.8	41.3	-83.2	3.3	7	-1.49	0.15	F6-F8

Table 4—Continued

Field [a] /Obs. Run	APS Star [b] Number	O Mag	$(O-E)$	$l[^\circ]$	$b[^\circ]$	V_{helio} km s^{-1}	σ_{helio} km s^{-1}	Number Lines	$[\frac{Fe}{H}]$ [c]	$\sigma_{[\frac{Fe}{H}]}$	Spec. Type
	3230839	16.2	0.6	39.6	41.6	-8.6	4.2	5	-1.87	0.16	G2
	2869663	16.9	0.6	40.3	41.3	-113.6	8.7	5	-1.76	0.15	F1
	3048975	17.3	0.8	39.9	41.6	-47.2	5.0	8	-2.10	0.29	G5-G8
	3054092	17.2	0.9	40.0	41.5	-65.9	4.0	7	-1.36	0.27	G2
	3442514	16.1	0.8	39.9	40.7	-16.8	5.4	6	-2.06	0.15	GO
	3417322	16.1	1.1	39.5	41.5	-18.0	3.5	9	-1.28	0.15	F6
P448/3	174263	16.5	0.6	39.7	29.7	26.1	3.0	7	-0.88	0.34	GO
	112446	16.2	0.8	40.6	30.0	-39.1	3.3	5	-1.26	0.17	A8-FO
	142973	16.0	0.5	40.2	29.9	-28.9	5.6	6	-1.07	0.35	G5
	111989	17.2	0.8	40.6	30.2	29.4	3.7	5	-1.39	0.15	F6-F8
	157446	17.0	0.7	39.9	30.3	52.0	6.6	6	-0.30	0.29	G2
	127354	16.9	0.7	40.5	30.2	131.1	6.5	4	...	...	A8-FO
	158805	17.6	0.9	40.1	29.7	-115.3	4.1	4	-1.94	0.20	G2
	174518	16.5	0.9	39.8	29.7	-75.7	6.5	6	-0.53	0.17	GO
	173605	16.4	0.5	39.6	30.0	-54.0	14.6	4	-0.66	0.38	GO
	142866	17.1	0.9	40.2	30.0	25.6	4.7	9	-1.33	0.35	G8
	111473	16.9	0.8	40.4	30.4	-67.9	11.0	5	-0.08	0.25	G8
	173496	16.0	0.8	39.5	30.0	-139.9	9.6	6	-0.50	0.31	G5
	189484	17.0	0.7	39.6	29.9	-161.2	1.7	4	-1.15	0.15	GO
	157077	16.4	0.6	39.7	30.4	-27.7	2.8	5	0.30	0.15	G5
	112600	17.1	0.6	40.6	30.0	-62.3	5.8	5	-0.88	0.34	GO
	143260	17.0	0.5	40.3	29.9	-18.0	7.5	4	-0.67	0.15	A8-FO
	173778	15.7	0.7	39.7	29.9	-6.8	3.5	5	-0.88	0.34	GO-G2
	158074	17.1	0.7	40.0	30.0	-31.4	5.1	7	-0.99	0.31	G7
	143010	17.5	0.9	40.2	30.0	-59.5	7.8	5	-0.30	0.29	G5
	142617	16.4	0.7	40.2	30.1	-121.6	3.7	7	-1.01	0.15	F2
	173301	17.0	0.9	39.6	30.2	-66.4	5.8	5	-0.42	0.35	G7
	157852	17.0	0.7	40.0	30.1	-97.6	9.5	4	-0.99	0.31	F5
	127621	17.1	0.8	40.5	30.1	-148.3	4.1	3	-2.10	0.15	A8-FO
	142362	16.7	0.8	40.0	30.2	-101.1	6.7	4	-1.66	0.15	F2
	141631	16.7	0.9	39.9	30.5	-61.6	4.2	7	-0.30	0.29	G7

Table 4—Continued

Field [a] /Obs. Run	APS Star [b] Number	O Mag	$(O-E)$	$l[^\circ]$	$b[^\circ]$	V_{helio} km s^{-1}	σ_{helio} km s^{-1}	Number Lines	$[\frac{Fe}{H}]$ [c]	$\sigma_{[\frac{Fe}{H}]}$	Spec. Type
	173452	15.7	0.6	39.6	30.1	-47.6	4.7	5	-0.69	0.37	G5
	172987	17.0	0.5	39.7	30.3	-40.7	4.9	5	-0.61	0.37	G5-G8
	142516	16.6	0.7	40.2	30.2	7.1	7.7	7	-1.23	0.15	F6
	159068	16.7	0.7	40.0	29.6	54.3	8.1	3	-1.35	0.29	F6-F8
	112668	16.4	0.5	40.6	30.0	-22.2	7.5	5	...	...	A8-FO
	157070	16.9	0.5	39.8	30.4	-38.1	8.0	5	-0.99	0.31	GO
	174352	17.2	0.3	39.8	29.7	55.0	7.5	8	...	...	A2
	111720	17.1	0.8	40.5	30.3	71.2	10.7	4	-1.49	0.15	F2
	158160	16.8	0.7	40.0	30.0	59.8	7.4	7	-0.06	0.27	G8
	142330	16.8	0.8	40.2	30.2	-39.6	7.8	4	-0.84	0.16	F8
	128253	16.7	0.9	40.5	29.8	-10.2	5.6	5	-0.68	0.17	F6-F8
	157925	16.6	0.8	40.0	30.1	75.9	5.7	3	-0.50	0.31	G5
	173345	16.4	0.5	39.6	30.1	-84.2	7.5	6	-1.03	0.28	GO
	157075	16.3	0.7	39.7	30.4	-33.3	6.2	5	-0.67	0.34	GO
	141723	17.1	0.8	39.9	30.5	-159.7	2.7	6	-1.65	0.15	F5
	156875	17.2	0.9	39.8	30.5	-36.2	4.2	3	-0.48	0.33	GO
	173213	16.7	0.6	39.6	30.2	-75.1	5.9	4	-0.46	0.35	GO
	158703	16.6	0.6	40.2	29.8	44.6	15.1	6	-0.64	0.28	GO
	141621	16.4	0.8	39.9	30.5	-1.0	7.1	9	-0.67	0.34	G8
	111440	16.1	0.7	40.4	30.4	-61.8	11.7	5	-1.80	0.15	G8
	128252	16.1	0.8	40.5	29.8	24.3	5.7	6	-1.20	0.28	F8
	143251	17.5	0.8	40.2	29.8	-25.4	4.6	5	-1.18	0.30	GO
	173015	16.1	0.8	39.7	30.3	29.7	3.8	5	-1.12	0.39	G8
	173106	16.0	0.8	39.6	30.2	23.2	4.5	5	-0.88	0.34	G5
	158220	16.3	0.6	39.9	29.9	-30.0	2.8	6	...	...	A1
	126738	16.4	0.9	40.3	30.4	6.8	2.4	5	-0.08	0.25	F9
	173328	16.9	0.4	39.6	30.1	-129.3	10.2	4	-0.98	0.15	F2
	158595	17.0	0.9	40.1	29.8	-93.5	7.9	5	-0.68	0.17	GO
	159044	16.2	0.9	40.1	29.6	-50.6	6.0	5	-0.67	0.21	GO
	173083	16.1	0.8	39.6	30.2	-96.5	8.3	7	-1.40	0.36	G8
	141843	16.7	0.8	39.9	30.4	-66.8	8.9	6	-1.35	0.29	GO

Table 4—Continued

Field [a] /Obs. Run	APS Star [b] Number	O Mag	$(O-E)$	$l[^\circ]$	$b[^\circ]$	V_{helio} km s^{-1}	σ_{helio} km s^{-1}	Number Lines	$[\frac{Fe}{H}]$ [c]	$\sigma_{[\frac{Fe}{H}]}$	Spec. Type
	142562	16.1	0.6	40.2	30.1	-295.7	3.8	5	...	...	A0
	142905	17.4	0.8	40.3	30.0	-68.3	2.8	4	-0.67	0.21	G2
	158086	16.1	0.6	39.9	30.0	-15.4	6.1	5	-0.67	0.15	F2
	157474	16.8	0.5	39.8	30.2	41.5	2.5	6	-0.44	0.20	G0
	158082	17.0	0.8	39.9	30.0	31.2	6.1	6	-0.69	0.37	GO
P505/3	989452	15.9	0.9	21.1	42.6	47.2	6.6	7	-0.88	0.34	G8
	1050335	15.9	0.5	20.8	42.7	-125.3	5.3	5	-1.75	0.24	GO
	1118830	16.3	1.0	20.8	42.2	-58.2	10.1	6	-1.83	0.35	G8
	1056160	16.7	1.0	21.1	42.3	-25.8	5.4	4	-1.33	0.35	G8
	989728	16.1	1.0	21.2	42.6	-45.3	10.2	6	-1.72	0.28	G8
	1113424	16.1	0.7	20.6	42.6	38.6	5.0	8	-1.35	0.29	G2
	989967	16.3	1.0	21.3	42.6	-72.5	5.8	7	-0.65	0.25	G8
	1056099	17.0	0.1	21.0	42.2	-250.6	2.9	5	-1.77	0.22	A8-F0
	1119351	16.2	0.9	20.8	42.1	-62.5	8.4	6	-1.40	0.36	G8
	1053566	17.4	0.8	20.8	42.4	-146.8	12.6	7	-1.50	0.24	GO
	1057908	17.3	1.0	21.1	42.1	4.2	12.6	6	-1.15	0.15	F8-GO
	1118915	16.9	0.9	20.9	42.2	-36.5	4.3	8	-0.85	0.25	G2
	1171489	15.9	0.9	20.4	42.3	-42.9	5.1	8	-0.67	0.34	G8
	1117098	17.0	1.1	20.7	42.3	-35.5	4.7	8	-0.64	0.15	G5
	1051485	16.0	0.5	20.7	42.6	-37.0	4.4	6	-1.50	0.24	G5-G8
	1116920	16.7	0.7	20.6	42.3	5.8	6.0	10	-0.50	0.31	G5
	991453	16.8	0.9	21.3	42.4	-17.2	6.0	5	-1.36	0.27	GO
	995077	15.9	0.5	21.5	42.2	1.9	8.9	6	-0.84	0.21	GO
	1117755	17.1	0.9	20.7	42.2	-39.7	8.3	6	-0.50	0.31	G8
	1118210	17.7	0.7	20.7	42.2	-43.8	11.2	4	-1.33	0.15	F8
	991200	17.1	0.9	21.1	42.4	1.4	6.2	8	-1.19	0.24	G2
	928048	17.2	1.0	21.5	42.5	20.0	6.4	6	-1.29	0.15	F2
	1115418	16.1	0.9	20.5	42.4	80.5	8.0	6	-0.88	0.39	G8
	987210	16.6	0.7	20.9	42.8	-108.3	4.4	6	-1.03	0.28	GO
	990788	16.9	1.0	21.4	42.5	-70.9	6.7	7	-1.50	0.24	G8
	1052197	16.4	0.7	20.9	42.6	-61.9	3.0	6	-0.50	0.31	G2

Table 4—Continued

Field [a] /Obs. Run	APS Star [b] Number	O Mag	$(O-E)$	$l[^\circ]$	$b[^\circ]$	V_{helio} km s^{-1}	σ_{helio} km s^{-1}	Number Lines	$[\frac{Fe}{H}]$ [c]	$\sigma_{[\frac{Fe}{H}]}$	Spec. Type
	1050252	16.1	0.8	20.7	42.7	-13.9	4.3	7	-1.67	0.33	G8
	1171160	15.9	0.9	20.4	42.3	-24.3	7.0	6	-1.51	0.29	G5
	989853	17.2	0.8	21.2	42.6	-38.1	8.5	6	-1.72	0.21	G8
	1115798	17.6	0.4	20.7	42.4	-93.5	9.9	7	-2.32	0.22	F2
	988459	17.1	0.4	21.2	42.7	44.4	4.6	11	-1.20	0.28	G0
	1053676	17.8	0.7	21.0	42.5	-175.5	1.7	4	-1.47	0.21	F8
	1119815	16.5	0.4	20.8	42.1	-111.4	5.8	9	-1.66	0.21	A8-F0
	989096	16.8	0.8	21.2	42.6	-84.8	6.2	7	-1.52	0.27	G2
	1119092	16.9	0.8	20.8	42.1	-143.6	7.4	5	-1.67	0.18	F4
	1120118	16.3	0.8	20.9	42.1	74.0	5.7	8	-1.03	0.28	G2
	987470	16.2	0.8	21.0	42.7	22.9	6.0	6	-1.35	0.29	GO
	991840	17.6	0.7	21.3	42.4	-22.8	4.9	5	-1.89	0.15	FO
	1116445	17.4	0.5	20.6	42.4	-72.9	3.4	6	-1.95	0.15	G8
	1114372	17.5	0.8	20.6	42.6	-139.0	7.5	5	-1.58	0.20	G5
	1051363	16.7	0.9	20.8	42.6	-83.8	5.5	9	-0.64	0.28	G5
	1115235	16.4	0.8	20.5	42.4	58.0	6.6	6	-1.96	0.15	F2
	1052830	16.0	0.6	20.9	42.5	11.2	2.9	5	-0.88	0.34	G8
	1054389	17.3	0.8	21.0	42.4	99.2	12.3	6	-1.43	0.17	GO
	1050376	16.1	0.7	20.7	42.7	-1.6	7.7	7	-1.47	0.21	F8-GO
	1052964	17.2	0.7	21.0	42.5	-94.8	8.1	5	-1.99	0.15	FO
	1054754	16.1	0.2	21.0	42.4	-97.0	10.4	9	-1.67	0.18	G0
	992659	16.3	0.9	21.3	42.3	-124.5	6.3	10	-1.35	0.29	GO
	1117063	17.1	0.9	20.6	42.3	-87.9	3.2	7	-1.35	0.29	G7
	1057355	16.4	0.9	21.2	42.2	-64.5	4.8	7	-1.33	0.35	G8
	1115514	17.1	0.4	20.7	42.5	-59.5	13.5	5	-1.75	0.16	G8
	1118414	16.2	0.7	20.8	42.2	-52.5	4.9	8	-0.99	0.31	G8
	987857	17.3	0.4	21.0	42.7	-39.4	6.5	5	-1.50	0.24	G8
	992191	16.4	1.0	21.3	42.4	-158.9	3.8	7	-1.07	0.35	G5-G8
	1057314	17.5	0.4	21.1	42.2	-38.1	7.2	4	...	...	A5
	1056689	16.2	0.8	21.0	42.2	79.9	7.2	8	-1.36	0.27	GO
	1115783	16.5	0.9	20.7	42.5	-22.1	4.5	6	-0.85	0.25	G5

Table 4—Continued

Field [a] /Obs. Run	APS Star [b] Number	O Mag	$(O-E)$	$l[^\circ]$	$b[^\circ]$	V_{helio} km s^{-1}	σ_{helio} km s^{-1}	Number Lines	$[\frac{Fe}{H}]$ [c]	$\sigma_{[\frac{Fe}{H}]}$	Spec. Type
	1051603	17.4	1.0	20.8	42.6	-46.6	3.0	10	-0.67	0.34	G8
	925450	16.8	1.0	21.3	42.7	44.7	11.1	5	-1.62	0.15	GO
	1054491	17.0	0.8	21.1	42.4	67.0	3.8	8	-1.35	0.29	GO
	1050536	15.9	0.8	20.9	42.7	20.0	3.9	7	-0.67	0.34	G5
	1058653	16.5	0.3	21.2	42.1	-88.2	13.8	4	-2.25	0.15	F0-F1
	1112258	15.8	0.2	20.3	42.6	-208.6	12.5	5	-2.37	0.17	F1-F2
	1117570	16.0	0.7	20.8	42.3	-56.5	4.6	9	-0.99	0.31	G5
P507/3	302956	16.4	0.9	30.8	32.4	32.2	7.8	4	-1.51	0.29	GO
	370569	16.2	0.8	30.7	31.7	-93.3	5.1	7	-1.18	0.30	GO
	309523	16.1	0.9	31.1	31.7	-149.7	5.9	6	-1.92	0.15	F8-GO
	306099	16.7	0.9	31.0	32.0	-35.4	4.3	6	-1.58	0.20	GO
	274042	17.4	0.8	31.3	32.1	-35.6	5.9	4	-0.07	0.19	GO
	340794	16.9	0.9	30.9	31.6	-38.6	3.7	7	-1.03	0.28	G8
	371126	16.0	0.6	30.8	31.7	-4.8	5.0	7	-0.57	0.16	F2
	368735	16.9	0.5	30.6	31.9	24.3	6.3	7	-0.84	0.16	G8
	342099	16.9	0.6	31.1	31.5	-66.0	5.5	9	0.01	0.29	G8
	338910	16.5	0.4	30.9	31.8	-43.2	4.5	9	0.06	0.24	G8
	310644	16.8	0.9	31.3	31.6	-54.3	5.7	9	0.21	0.21	G8
	276222	17.5	0.8	31.3	31.8	1.0	6.3	5	-1.62	0.15	F2-F5
	272230	16.8	0.7	31.1	32.3	27.9	5.5	3	-0.85	0.25	F6-F8
	401891	17.7	0.8	30.4	31.9	-127.3	1.2	3	-0.53	0.17	G8
	369259	16.0	0.6	30.6	31.8	-170.7	4.1	10	-1.90	0.15	A8-FO
	336027	16.7	0.8	30.7	32.1	-108.2	7.4	5	-1.00	0.16	F5
	402468	17.5	0.5	30.4	31.8	23.5	4.9	5	-0.84	0.15	G5-G8
	275061	16.3	0.7	31.3	31.9	-0.9	5.9	9	-1.18	0.37	G8
	308363	16.1	0.7	31.1	31.8	-147.3	6.3	7	-1.20	0.28	F6
	276503	17.2	0.8	31.4	31.8	-130.5	5.9	5	-0.53	0.17	GO
	309429	17.3	1.0	31.1	31.7	70.1	9.2	3	-1.15	0.15	GO
	306370	17.2	1.0	31.0	32.0	-78.9	3.4	9	-0.50	0.31	G8
	310549	16.8	0.9	31.3	31.7	-97.1	4.4	5	-0.68	0.17	G5
	310291	17.1	0.7	31.3	31.7	61.9	5.4	5	-0.44	0.20	G5-G8

Table 4—Continued

Field [a] /Obs. Run	APS Star [b] Number	O Mag	$(O-E)$	$l[^\circ]$	$b[^\circ]$	V_{helio} km s^{-1}	σ_{helio} km s^{-1}	Number Lines	$[\frac{Fe}{H}]$ [c]	$\sigma_{[\frac{Fe}{H}]}$	Spec. Type
	367408	16.5	0.9	30.4	32.0	-140.0	7.1	6	-1.03	0.38	G8
	305153	16.6	0.9	31.0	32.1	0.8	5.8	5	-1.34	0.30	G2-G5
	334164	17.2	0.8	30.6	32.4	-54.4	8.1	4	-0.30	0.31	G5
	368793	16.8	0.8	30.7	31.9	-76.6	4.6	6	-0.48	0.33	G8
	306265	16.2	0.8	31.0	32.0	-55.6	5.3	5	-1.20	0.28	GO
	366918	16.8	0.8	30.5	32.1	20.6	6.0	7	-0.44	0.27	F9
	305514	16.0	0.5	31.0	32.1	36.9	9.7	4	-0.85	0.25	F9
	341398	17.3	0.9	31.0	31.6	21.4	5.2	4	-1.15	0.15	F8
	306979	15.8	0.6	31.0	31.9	47.9	6.1	7	-0.69	0.15	GO
	335093	17.6	0.6	30.6	32.3	-217.1	3.8	4	-2.36	0.15	F2-F5
	305368	16.1	0.7	31.0	32.1	-1.2	2.6	8	-0.44	0.20	G5
	371309	16.4	0.8	30.7	31.6	-54.9	4.6	5	-0.85	0.25	G5
	371159	16.3	0.9	30.6	31.6	-67.5	6.0	8	-0.88	0.34	G5
	271676	16.9	0.8	31.0	32.4	24.6	4.8	6	-0.69	0.37	G8
	307393	16.4	0.9	31.0	31.9	-47.6	4.6	7	-0.67	0.34	G8
	369199	17.5	0.8	30.6	31.9	32.1	2.6	4	-1.57	0.30	G8
	336261	17.5	0.9	30.7	32.1	-34.9	7.9	4	-1.26	0.38	G8
	303081	16.3	0.9	30.7	32.3	19.4	2.2	7	-0.84	0.29	G5
	305715	16.1	0.8	30.9	32.0	24.6	1.9	6	-0.64	0.28	G2-G5
	337141	17.3	0.6	30.7	32.0	-64.6	1.6	4	-0.85	0.25	G5-G8
	271608	16.4	0.8	31.0	32.3	79.5	3.2	4	-1.90	0.30	G2
	273338	16.1	0.7	31.2	32.2	-35.9	4.5	7	-0.86	0.15	F2
	303813	16.9	0.9	30.8	32.2	36.6	3.4	4	-0.84	0.29	G8
	303291	16.9	0.4	30.9	32.4	-64.5	8.9	7	-0.84	0.29	G8
	271672	15.9	0.2	31.2	32.4	23.7	2.3	8	-0.49	0.15	F5
	339517	16.6	0.3	30.9	31.8	-15.9	5.5	5	...	...	A0-A1
	309716	17.2	0.8	31.1	31.7	-87.8	11.9	6	-1.26	0.15	F5-F6
	369130	17.1	0.8	30.6	31.9	-113.3	9.2	5	-1.03	0.25	F8
	310589	16.5	0.8	31.2	31.6	-76.9	3.8	6	-0.99	0.31	G8
	337166	17.0	0.7	30.7	32.0	-289.4	9.3	7	-2.60	0.19	A8-FO
	404694	17.0	0.8	30.6	31.6	-153.4	8.1	7	-0.49	0.15	F5

Table 4—Continued

Field [a] /Obs. Run	APS Star [b] Number	O Mag	$(O-E)$	$l[^\circ]$	$b[^\circ]$	V_{helio} km s^{-1}	σ_{helio} km s^{-1}	Number Lines	$[\frac{Fe}{H}]$ [c]	$\sigma_{[\frac{Fe}{H}]}$	Spec. Type
	272087	17.1	0.9	31.2	32.4	-28.1	6.0	5	-1.03	0.40	G5-G8
	302400	16.8	0.7	30.8	32.4	-134.9	5.8	9	-1.07	0.35	G8
	337176	17.1	0.7	30.7	32.0	-34.7	4.0	4	-0.84	0.29	G5
	307679	17.4	1.0	31.2	31.9	68.4	4.3	5	-0.48	0.33	G8
	341859	16.8	0.5	31.1	31.5	-48.9	6.2	6	-0.77	0.15	G5
	367278	17.3	0.9	30.5	32.0	69.0	7.3	7	-0.84	0.16	F8-GO
	305740	16.9	0.9	31.0	32.1	-75.5	10.0	5	-1.48	0.33	GO
	303243	15.9	0.6	30.8	32.3	-49.7	3.4	9	-0.85	0.25	G2-G5
	304817	17.0	0.7	30.9	32.1	114.9	4.7	5	-1.03	0.28	G8
	404168	16.8	0.8	30.5	31.6	27.8	5.1	6	-1.90	0.30	G8
	337338	16.8	0.7	30.9	32.0	-188.8	9.1	5	-1.66	0.15	F1
	369490	17.3	0.8	30.7	31.8	-155.2	7.8	6	-1.02	0.21	G2-G5
P566/3	1201507	17.1	0.9	20.5	32.4	69.1	9.9	7	0.06	0.24	G8
	1518353	17.1	0.9	19.8	32.3	-66.6	4.7	5	-1.51	0.29	G8
	1204506	16.5	0.5	20.7	32.2	-26.1	3.8	9	-1.64	0.26	G5
	1308177	16.9	0.5	20.3	32.2	72.5	5.0	7	-1.18	0.20	F6
	1312427	17.5	0.9	20.5	32.0	-339.0	9.2	6	-1.66	0.27	GO
	1521278	17.0	0.2	19.9	32.1	18.3	4.2	4	-0.59	0.15	F6
	1302789	15.8	0.4	20.1	32.4	28.4	4.0	9	-0.88	0.34	G5
	1301996	16.5	-0.2	20.1	32.5	-26.7	4.7	5	-1.35	0.22	GO
	1412385	17.2	0.5	19.9	32.2	60.8	10.5	6	-2.02	0.15	F2
	1198476	16.3	0.7	20.4	32.5	-53.3	6.7	7	-0.69	0.15	F8
	1526687	16.8	0.1	20.1	31.9	-43.3	3.7	5	-0.64	0.28	G8
	1303029	17.2	0.8	20.2	32.4	-73.7	3.5	7	-0.44	0.27	F8
	1308434	17.7	0.6	20.4	32.2	16.8	3.3	5	-0.59	0.15	F3-F5
	1410003	17.1	0.8	19.9	32.4	12.4	2.8	4	-2.02	0.15	F2
	1520686	16.9	0.4	19.9	32.2	-44.4	3.5	4	-1.49	0.15	F6
	1418626	16.6	0.9	20.3	32.0	33.0	5.1	4	-0.85	0.25	G0
	1411583	16.9	0.9	20.0	32.3	-78.9	5.8	8	-1.94	0.20	G8
	1304475	16.1	0.5	20.2	32.4	-23.3	3.2	8	-1.67	0.33	G8
	1311153	17.3	0.5	20.5	32.1	-45.4	6.2	5	-1.03	0.28	F8

Table 4—Continued

Field [a] /Obs. Run	APS Star [b] Number	O Mag	$(O-E)$	$l[^\circ]$	$b[^\circ]$	V_{helio} km s^{-1}	σ_{helio} km s^{-1}	Number Lines	$[\frac{Fe}{H}]$ [c]	$\sigma_{[\frac{Fe}{H}]}$	Spec. Type
	1416484	17.0	0.7	20.2	32.1	61.3	12.3	5	-1.36	0.27	GO
	1518551	17.3	0.8	19.7	32.2	79.2	6.6	5	-0.84	0.29	G2
	1520575	16.4	0.7	19.9	32.2	7.2	3.6	6	-1.75	0.16	F8-GO
	1303734	17.6	0.7	20.3	32.5	-55.9	5.6	4	-1.48	0.15	F2
	1420023	17.1	0.8	20.3	31.9	57.3	7.4	7	...	...	F5
	1308021	17.0	0.7	20.5	32.2	-24.0	2.2	7	...	...	G8
	1316953	16.0	0.5	20.5	31.8	-33.6	3.3	6	-2.25	0.15	GO
P5661/3	1517435	16.4	0.8	19.7	32.3	-12.4	1.8	6	...	...	G5
	1306264	16.8	0.9	20.3	32.3	53.9	10.0	5	-1.97	0.15	F8
	1410915	15.8	0.5	19.9	32.3	93.3	8.2	7	-0.34	0.18	GO
	1526695	17.1	0.8	20.1	31.9	77.5	4.1	5	-2.21	0.15	GO
	1522528	16.6	0.4	19.9	32.1	5.0	2.0	5	-1.36	0.27	GO
	1423431	16.6	0.6	20.4	31.8	34.7	5.0	6	-2.17	0.15	F5
	1528525	16.7	0.5	20.2	31.8	26.6	7.8	5	-1.19	0.24	F8
	1303299	17.2	0.6	20.2	32.4	-20.2	5.0	5	-1.03	0.28	F8
	1304014	15.9	0.5	20.2	32.4	-24.4	0.5	5	-1.66	0.27	G5
	1620300	16.6	0.7	19.7	32.0	-18.0	4.2	7	-0.99	0.31	G5
	1522771	16.0	0.8	20.0	32.1	-14.3	3.5	5	-0.67	0.34	G2-G5
	1203516	16.4	0.8	20.6	32.3	-18.0	4.4	7	-1.67	0.33	G5-G8
	1209857	16.4	0.1	20.7	32.0	-52.6	9.1	6	-1.98	0.15	F5-F6
	1525978	16.4	0.3	20.0	31.9	-55.5	8.4	7	-1.58	0.20	G5
	1308697	17.4	0.4	20.4	32.2	-168.1	8.2	6	-1.03	0.28	G5
	1415253	16.5	0.4	20.2	32.1	45.1	6.0	7	-0.84	0.29	G5
	1307069	17.4	0.7	20.3	32.2	-185.5	7.2	4	-1.87	0.23	GO
	1306053	17.3	0.9	20.3	32.3	-33.6	6.1	8	-1.20	0.28	G5
	1521122	15.8	0.6	19.8	32.1	23.7	2.2	7	-0.99	0.31	G8
	1301175	16.7	0.7	20.1	32.5	-170.9	9.0	8	-1.65	0.15	F8
	1409023	16.0	0.6	19.9	32.4	-162.5	6.8	8	-1.67	0.18	F8
	1522070	16.3	0.7	19.8	32.0	-30.0	6.0	6	-1.87	0.37	G5-G8
	1201015	16.1	0.8	20.6	32.4	4.0	4.3	7	-1.34	0.30	GO-G2
	1618901	16.2	0.5	19.7	32.1	32.4	6.6	6	-0.50	0.31	GO

Table 4—Continued

Field [a] /Obs. Run	APS Star [b] Number	O Mag	$(O-E)$	$l[^\circ]$	$b[^\circ]$	V_{helio} km s^{-1}	σ_{helio} km s^{-1}	Number Lines	$[\frac{Fe}{H}]$ [c]	$\sigma_{[\frac{Fe}{H}]}$	Spec. Type
	1517880	16.6	0.8	19.7	32.3	40.3	5.2	4	-0.67	0.34	G5
	1419701	16.5	0.7	20.3	31.9	-123.7	7.0	6	-1.18	0.30	G5
	1408750	16.7	0.6	19.8	32.4	-39.7	3.5	5	-1.35	0.29	G2-G5
	1528266	16.0	0.6	20.1	31.8	-165.3	9.0	8	-0.30	0.29	G2
	1303429	16.8	0.0	20.2	32.4	-262.0	6.4	8	...	...	F2
	1308890	16.4	0.8	20.3	32.1	31.1	6.9	8	-1.66	0.27	G2-G5
	1204193	15.7	0.7	20.5	32.2	33.5	4.5	6	-0.65	0.25	G5
	1521514	16.7	0.1	19.9	32.1	21.4	4.3	4	-1.00	0.16	F6
	1304747	16.7	0.4	20.1	32.3	-42.8	6.0	7	0.00	0.17	GO-G2
	1206416	16.6	0.9	20.6	32.1	-33.5	4.9	9	-1.69	0.40	G8
	1414737	16.3	0.6	20.0	32.1	-136.1	8.6	10	-0.61	0.37	G5
	1313312	16.9	0.5	20.4	31.9	56.7	2.2	6	-0.13	0.27	F8-GO
	1519659	16.1	0.6	19.8	32.2	50.4	5.8	12	-1.35	0.29	GO
	1528209	15.9	0.6	20.0	31.7	78.1	5.5	6	0.02	0.17	GO
	1521930	16.4	0.0	20.0	32.1	69.2	14.6	5	-2.98	0.29	FO
	1419307	16.3	0.9	20.3	31.9	13.8	5.1	6	-2.08	0.34	G5
	1422838	16.2	0.7	20.4	31.8	42.6	7.4	7	-0.64	0.28	G2-G5
P5661/ 2,3	1409761	15.8	0.6	19.9	32.4	-87.3	10.5	6	-0.13	0.19	G0-G2 (
	1409751	16.7	0.7	20.0	32.4	21.6	4.3	7	-0.65	0.25	GO-G2
	1306753	16.2	0.5	20.3	32.3	-73.5	7.0	5	-1.33	0.35	G2-G5
	1307401	16.8	0.7	20.4	32.2	-22.5	6.4	5	-0.69	0.15	F8-GO
	1409061	16.9	0.6	20.0	32.4	-77.6	6.0	6	-1.23	0.15	F8
	1417636	16.6	0.6	20.1	32.0	52.8	5.3	6	...	...	A8-FO
	1418646	16.5	0.3	20.2	31.9	-27.4	2.9	6	-2.04	0.15	F5
	1419307	16.3	0.9	20.3	31.9	43.9	3.6	6	-2.08	0.34	G5
P5661/3	1299726	15.9	0.2	20.1	32.6	-219.6	8.0	11	-0.84	0.16	GO-G2
	1525017	16.1	0.7	20.0	31.9	-265.0	3.6	7	-0.50	0.31	G2-G5
P566/1	1409317	16.6	0.5	19.9	32.4	-219.6	8.0	11	-1.36	0.27	F8-G0
	1524681	17.0	0.7	20.0	31.9	-26.5	3.6	7	...	...	G8
	1418648	17.2	0.8	20.2	31.9	-79.6	7.0	7	-1.34	0.30	G2-G5
	1418626	16.6	0.9	20.3	32.0	-19.2	6.4	6	...	...	G0

Table 4—Continued

Field [a] /Obs. Run	APS Star [b] Number	O Mag	$(O-E)$	$l[^\circ]$	$b[^\circ]$	V_{helio} km s^{-1}	σ_{helio} km s^{-1}	Number Lines	$[\frac{Fe}{H}]$ [c]	$\sigma_{[\frac{Fe}{H}]}$	Spec. Type
	1303022	17.3	0.6	20.1	32.4	-37.6	8.5	9	-0.79	0.39	GO
	1416179	16.7	0.7	20.1	32.1	30.3	5.3	7	-2.16	0.15	G2-G5
	1308762	16.9	0.8	20.3	32.1	27.2	6.1	8	...	...	G5
P566/2	1524096	16.0	0.6	20.0	32.0	127.0	11.7	4	···	···	G0
	1311223	16.0	0.7	20.4	32.0	-29.5	4.9	5	···	···	FO
	1413646	16.6	0.2	20.0	32.2	-25.2	3.8	11	···	···	G5
	1524987	16.4	0.7	20.0	31.9	-46.2	5.6	11	···	···	G5
	1418021	16.8	0.5	20.3	32.0	58.1	3.8	7	···	···	G5
	1304852	15.8	0.6	20.1	32.3	-28.1	2.5	4	···	···	G5
P566/ 1,3	1411521	16.9	0.5	20.0	32.3	-119.6	5.7	11	-2.40	0.15	G2-G5
	1414424	17.1	0.5	20.1	32.1	55.9	4.9	7	-0.48	0.33	G5
	1524045	16.6	0.9	20.0	32.0	-118.2	10.8	3	-0.99	0.31	G8
	1523665	17.2	0.7	20.0	32.0	-38.1	6.2	7	-2.02	0.20	G2-G5
	1200164	16.7	0.1	20.4	32.4	33.6	6.4	3	-1.67	0.15	F0-F2
	1303770	16.9	0.6	20.2	32.4	-54.7	6.1	5	-0.13	0.19	GO
	1305182	16.9	0.3	20.3	32.3	-53.6	5.7	5	...	...	A2
	1306268	17.0	0.8	20.3	32.3	77.6	6.4	4	-1.26	0.38	G5
	1306533	16.8	0.7	20.2	32.2	-55.6	7.1	7	-2.05	0.15	G5
	1306618	17.0	0.7	20.3	32.3	-34.9	7.3	5	-0.88	0.34	GO-G2
	1307315	16.7	0.7	20.3	32.2	-53.0	5.1	8	-1.93	0.23	G5
	1309219	16.8	0.9	20.3	32.1	-22.9	3.7	6	-0.50	0.15	GO-G2
	1310293	17.1	0.8	20.4	32.1	40.9	2.4	6	-1.50	0.24	GO
	1411271	16.7	0.8	20.1	32.4	-107.0	5.8	10	-1.85	0.27	G2-G5
	1411275	16.8	0.3	19.9	32.3	-63.7	3.2	4	-1.07	0.35	G5
	1413202	16.6	0.8	20.0	32.2	-127.7	6.4	10	-2.05	0.15	GO
	1415740	16.6	0.7	20.0	32.0	-63.7	4.4	8	-0.65	0.25	F8-G0
	1522520	16.7	0.4	19.9	32.1	-29.9	4.7	7	-1.07	0.35	G5
P566/ 2,3	1410591	16.4	0.3	19.9	32.3	44.0	4.4	6	-1.03	0.25	G2
	1411978	16.8	0.7	19.9	32.2	19.5	3.3	6	-1.12	0.39	G5
	1305296	16.5	0.4	20.3	32.3	74.8	2.0	5	-1.03	0.28	GO
	1200523	16.1	0.8	20.4	32.4	-28.5	5.7	7	-1.48	0.33	G5

Table 4—Continued

Field [a] /Obs. Run	APS Star [b] Number	O Mag	$(O-E)$	$l[^\circ]$	$b[^\circ]$	V_{helio} km s^{-1}	σ_{helio} km s^{-1}	Number Lines	$[\frac{Fe}{H}]$ [c]	$\sigma_{[\frac{Fe}{H}]}$	Spec. Type
	1204328	16.3	0.8	20.6	32.2	20.9	3.7	7	-1.18	0.20	F8-GO
	1409346	16.1	0.4	20.0	32.4	-26.9	4.3	7	-1.18	0.30	G5
	1409378	16.4	0.8	19.9	32.4	-55.5	1.1	8	-0.97	0.39	G8
	1410481	16.2	0.6	20.0	32.4	-41.7	2.3	8	-0.30	0.31	G5-G8
	1412635	15.7	0.8	20.0	32.2	-38.2	5.5	7	0.01	0.18	G2
	1415299	15.9	0.9	20.1	32.1	-70.8	4.2	9	-1.24	0.37	G8-G9
	1417510	16.1	0.7	20.3	32.0	43.6	2.6	6	-1.02	0.21	F8
	1521549	16.2	0.8	19.8	32.1	-20.8	2.0	5	-1.07	0.35	G8
	1521957	16.0	0.0	19.9	32.1	156.2	2.4	6	-1.73	0.15	F2
	1523212	15.9	0.5	20.0	32.0	-46.1	4.0	8	-0.67	0.34	G5
	1524778	16.2	0.9	20.0	31.9	-64.4	4.5	10	-1.53	0.41	G8
	1526803	15.9	0.9	20.1	31.9	-48.8	2.8	11	-0.67	0.21	G8
	1527255	16.5	0.4	20.2	31.9	-53.8	8.1	4	-0.28	0.20	GO
P741/1	576992	16.7	1.0	338.8	41.3	-142.2	4.6	6	-1.52	0.27	GO
	618411	17.0	0.7	338.6	40.8	-28.9	3.5	4	-0.53	0.17	F9
	619302	16.6	0.6	339.0	40.7	-106.2	8.0	5	-1.93	0.23	G5
	577897	16.5	0.9	339.1	41.2	-53.1	5.9	7	-2.25	0.15	G8
	578636	16.6	0.9	339.2	41.0	47.5	3.4	3	-1.77	0.26	G5
	600358	17.0	0.6	339.1	40.8	-65.5	1.4	4	-1.50	0.24	G5
	598327	16.8	1.0	338.6	41.1	-22.4	6.0	5	-0.11	0.17	F8-GO
	635708	16.5	1.0	338.6	40.7	87.6	4.8	6	-1.33	0.35	G8
	598694	17.3	1.0	338.6	41.1	-43.9	6.0	4	-0.46	0.35	G2
	599493	17.0	0.7	339.0	41.0	-25.1	4.5	4	-1.15	0.15	G2
	636105	16.9	0.9	338.7	40.6	-28.5	5.5	5	-1.64	0.26	GO
	599621	17.5	1.0	338.9	40.9	-153.5	7.8	8	-1.33	0.35	G8
	598664	16.9	0.9	338.6	41.1	-63.4	3.3	5	-1.11	0.15	F8
	618747	16.8	0.9	338.9	40.8	-42.8	1.7	7	-1.36	0.27	GO
	618629	16.6	0.7	338.6	40.8	-110.8	3.7	7	-1.20	0.28	G8
	578057	16.5	1.0	339.1	41.1	-30.9	5.6	5	-1.59	0.40	G8
	617876	16.8	1.0	338.5	40.9	-20.7	3.9	6	-0.99	0.31	G8
	635773	16.8	0.4	338.6	40.7	-15.6	1.4	5	-1.36	0.27	GO

Table 4—Continued

Field [a] /Obs. Run	APS Star [b] Number	O Mag	$(O-E)$	$l[^\circ]$	$b[^\circ]$	V_{helio} km s^{-1}	σ_{helio} km s^{-1}	Number Lines	$[\frac{Fe}{H}]$ [c]	$\sigma_{[\frac{Fe}{H}]}$	Spec. Type
	636170	16.8	0.8	338.7	40.6	-28.5	3.4	4	-0.67	0.21	GO
	576621	16.8	0.9	338.8	41.3	-155.4	9.2	5	-1.20	0.28	GO
	599158	16.7	0.9	338.9	41.1	-45.3	5.7	6	-1.35	0.29	G5
	598203	16.9	1.0	338.6	41.1	-41.9	4.5	5	-1.10	0.33	G8
	618163	16.8	1.0	338.7	40.9	-70.3	3.7	9	-1.57	0.30	G8-G9
	600408	16.6	0.9	339.1	40.8	-86.0	5.4	7	-2.09	0.16	G8
	600085	17.3	0.8	339.1	40.8	-105.6	6.1	6	-2.00	0.17	G8
	619223	17.3	0.5	338.9	40.6	-136.0	10.3	3	-2.08	0.15	A8-FO
	619237	16.7	0.8	339.0	40.7	-77.3	7.0	5	-1.47	0.21	GO
	599960	17.5	0.8	339.0	41.0	-70.4	7.1	6	-2.19	0.18	G8
P741/2	619452	15.8	1.0	339.2	41.0	-32.0	4.2	6	···	···	G8
	577055	15.8	0.8	340.0	42.6	-92.7	7.2	5	···	···	G5
	618264	16.3	0.7	338.9	41.2	-42.8	5.8	5	···	···	G8
	598948	16.4	0.7	340.1	42.6	-57.6	5.2	4	···	···	GO
	577534	15.9	0.8	340.1	42.5	25.0	4.3	4	···	···	G8
	619155	16.2	0.8	339.2	41.1	-53.8	4.5	8	···	···	G8
	618944	16.1	1.0	339.0	41.0	7.8	3.8	5	···	···	G8
	618539	17.3	0.9	339.0	41.2	32.9	5.0	5	···	···	G8
	578415	16.0	0.8	340.3	42.4	-58.8	7.8	7	···	···	GO
	600025	16.5	0.6	340.4	42.5	101.2	3.3	5	···	···	FO
	598234	16.0	0.7	340.0	42.7	-41.8	4.6	7	···	···	G2
	578640	15.8	1.0	340.4	42.4	39.3	4.7	6	···	···	G8
	599180	15.7	0.9	340.2	42.5	-63.7	3.7	7	···	···	G8
	598907	16.1	1.0	338.8	41.0	-50.4	7.0	7	···	···	G8
	600237	15.6	1.0	340.5	42.5	-49.6	6.5	5	···	···	G8
	600054	16.2	0.7	339.1	40.9	166.0	8.6	5	···	···	F8
	617781	16.1	0.8	338.7	41.2	-105.4	4.6	5	···	···	F8
	599421	16.1	1.1	340.3	42.6	-23.6	4.0	4	···	···	G2
	618192	16.1	0.5	338.9	41.2	-29.4	2.8	6	···	···	F4
	599092	15.8	1.0	340.2	42.6	-40.7	6.1	5	···	···	F8-GO
	599069	16.4	1.0	340.1	42.6	141.2	5.9	5	···	···	G2

Table 4—Continued

Field [a] /Obs. Run	APS Star [b] Number	O Mag	$(O-E)$	$l[^\circ]$	$b[^\circ]$	V_{helio} km s^{-1}	σ_{helio} km s^{-1}	Number Lines	$[\frac{Fe}{H}]$ [c]	$\sigma_{[\frac{Fe}{H}]}$	Spec. Type
	599220	15.8	0.1	338.9	41.0	64.6	9.4	3	···	···	A1
	598281	16.0	1.0	338.6	41.1	-59.4	5.8	10	···	···	G8
	636102	15.8	0.8	339.1	41.2	-25.3	2.5	5	···	···	F8-GO
	635594	15.8	1.0	338.9	41.3	-33.5	2.6	9	···	···	G8
P741/1,2	577483	16.8	0.9	338.9	41.1	30.1	3.5	7	-1.67	0.18	G2
	578636	16.6	0.9	339.2	41.0	47.3	2.9	3	-1.77	0.26	G5
	599278	16.9	0.9	338.9	41.1	-125.0	4.2	5	-1.00	0.16	GO
	599318	16.7	0.9	338.9	41.1	-85.8	4.4	8	-1.18	0.37	G8
	599506	16.5	0.8	339.0	41.0	-163.6	4.1	5	-0.99	0.31	G2
	599595	16.7	0.8	339.0	41.0	-83.6	3.5	4	-1.10	0.33	G8
	599975	16.5	0.8	338.9	40.9	-58.5	3.7	4	-1.86	0.15	G2-G5
	600107	16.7	0.7	339.1	40.9	-108.5	5.3	7	-0.69	0.15	G2
	618559	16.5	0.9	338.6	40.8	-58.9	5.9	5	-1.87	0.16	GO-G2
	618971	16.9	0.9	338.8	40.7	36.6	2.4	8	-0.50	0.31	G2-G5
	635958	17.4	1.0	338.7	40.7	-35.2	3.0	5	-1.77	0.26	G8
P799/1	1221645	16.9	0.9	319.9	41.2	37.3	6.4	4	...	...	G5
	1289841	17.0	0.7	319.8	40.9	34.7	8.8	6	-0.28N	0.20	GO-G2
	1158419	17.0	0.9	320.1	41.3	-47.9	5.9	5	-1.94	0.20	G8
	1159270	17.1	0.9	320.3	41.3	-46.8	4.6	6	...	...	G2-G5
	1294676	16.5	0.9	320.3	40.9	-41.0	4.5	5	-0.44	0.27	GO
	1292280	16.8	0.9	319.9	40.8	33.4	3.6	7	-0.67	0.34	G5-G8
	1159595	16.8	0.8	320.3	41.2	-30.9	5.8	5	-0.79	0.39	G8
	1288496	17.6	0.7	319.6	41.1	-66.3	2.8	6	0.30	0.15	G0-G2
	1221164	17.7	0.7	319.8	41.1	91.0	7.2	4	...	...	G0-G2
	1224664	17.0	0.7	320.2	41.2	29.2	5.2	5	-1.11N	0.15	F8
	1159380	17.4	0.7	320.3	41.2	2.4	4.0	5	...	...	GO-G2
	1291367	17.4	0.9	320.0	41.0	-38.8	3.2	5	-1.36N	0.27	G2
	1220782	17.3	0.8	319.7	41.3	69.1	7.7	6	-1.57	0.15	F6
	1291084	17.3	0.6	320.0	40.9	18.8	3.2	8	...	...	GO
	1288853	17.4	0.8	319.6	41.0	103.8	4.2	6	-0.71N	0.15	F5
	1291239	17.6	0.9	320.0	40.9	-43.5	8.4	6	-1.20	0.28	G5

Table 4—Continued

Field [a] /Obs. Run	APS Star [b] Number	O Mag	$(O-E)$	$l[^\circ]$	$b[^\circ]$	V_{helio} km s^{-1}	σ_{helio} km s^{-1}	Number Lines	$[\frac{Fe}{H}]$ [c]	$\sigma_{[\frac{Fe}{H}]}$	Spec. Type
	1291902	16.8	0.9	320.0	40.9	-108.5	15.4	4	-2.95	0.35	F0-F2
	1221396	17.4	0.3	319.9	41.2	141.0	8.0	5	-0.69	0.15	A5-A8
	1157704	17.4	0.7	319.9	41.3	-79.6	7.1	4	...	...	F8-GO
	1222619	16.6	1.0	320.0	41.0	-125.5	3.4	7	-0.79N	0.39	G8
	1365826	16.8	0.9	319.9	40.8	-63.5	9.0	5	-1.94:	0.20	G2-G5
	1223286	16.9	1.0	320.0	41.1	-41.0	5.0	4	-2.45	0.15	GO-G2
	1288630	16.7	1.0	319.6	40.9	31.0	3.5	5	...	...	G5
	1293341	17.1	1.0	320.1	40.9	-12.8	3.0	6	-2.25	0.15	G2-G5
	1293021	17.0	0.8	320.1	40.8	-45.1	8.5	4	-2.10	0.15	G5
	1288105	17.6	0.8	319.6	41.1	-59.4	3.5	4	-3.23	0.15	G5
	1224605	16.7	0.9	320.2	41.2	-80.9	4.3	7	-2.82:	0.19	G5-G8
P799/2	1224472	16.3	1.0	320.8	42.3	7.6	3.1	5	···	···	G5-G8
	1367956	16.2	0.8	320.8	42.7	-44.3	5.2	7	···	···	G5
	1158565	16.1	0.9	320.5	42.3	-115.3	3.6	8	···	···	G5
	1368762	16.3	0.6	320.9	42.7	132.2	8.2	4	···	···	F8-GO
	1290289	16.1	0.8	320.5	42.8	42.3	10.0	6	···	···	F2
	1222762	16.2	0.5	320.5	42.4	-61.2	6.0	6	···	···	F5
	1221357	16.4	1.0	320.4	42.6	-59.9	2.8	5	···	···	GO
	1223425	16.4	0.9	320.6	42.4	11.8	2.8	5	···	···	G5
	1225019	16.3	1.0	320.8	42.3	86.4	4.9	4	···	···	GO
	1157988	16.0	0.9	320.4	42.3	-45.7	4.0	6	···	···	G8
	1292555	16.2	0.8	320.7	42.6	130.1	9.2	4	···	···	G8
	1222696	17.2	0.8	320.5	42.4	81.6	5.1	5	···	···	G8
	1288563	16.3	0.8	320.3	42.7	-111.4	5.6	7	···	···	G8
	1287315	15.9	1.0	320.1	42.7	223.1	2.6	5	···	···	FO-F2
	1158462	15.7	1.0	320.5	42.3	-39.6	4.9	7	···	···	G8
	1290994	16.3	1.0	320.6	42.7	-32.8	2.2	4	···	···	G5
	1292015	16.0	0.6	320.7	42.6	47.9	5.7	5	···	···	F8-GO
	1156485	15.8	0.8	320.2	42.3	-83.0	3.6	4	···	···	GO
	1222714	17.6	0.9	320.5	42.5	-68.0	4.2	5	···	···	G5-G8
	1221698	16.8	1.0	320.4	42.4	-77.3	3.9	8	···	···	G5

Table 4—Continued

Field [a] /Obs. Run	APS Star [b] Number	O Mag	$(O-E)$	$l[^\circ]$	$b[^\circ]$	V_{helio} km s^{-1}	σ_{helio} km s^{-1}	Number Lines	$[\frac{Fe}{H}]$ [c]	$\sigma_{[\frac{Fe}{H}]}$	Spec. Type
	1159139	16.0	0.9	320.6	42.2	29.1	4.6	6	···	···	G5
	1220735	15.6	1.0	320.3	42.6	-62.8	3.1	9	···	···	G2
	1288785	16.9	0.7	320.4	42.8	73.9	7.3	3	···	···	F2
	1287618	15.7	0.8	320.2	42.6	28.6	1.8	5	···	···	G5
	1294767	16.3	1.0	320.9	42.5	-96.4	8.6	8	···	···	GO
	1224627	16.4	0.7	320.8	42.4	44.2	6.7	4	···	···	F6
	1291610	15.8	0.9	320.6	42.7	25.2	4.6	5	···	···	F8-GO
	1290516	16.3	0.9	320.5	42.6	38.3	5.6	4	···	···	F2
P799/1,2	1158333	16.6	0.9	320.1	41.3	-32.5	3.5	5	-0.88	0.34	G2-G5
	1159299	16.5	0.5	320.3	41.3	-42.1	2.7	7	-1.99N	0.15	GO
	1223623	16.9	1.0	320.2	41.1	-52.6	4.7	7	-1.86	0.15	GO-G2
	1290045	16.7	1.1	319.8	40.9	122.8	3.5	6	-1.51N	0.15	F6
	1292010	16.9	0.5	320.0	40.9	-61.2	3.8	6	-0.65	0.25	GO-G2
	1294234	17.7	0.4	320.3	40.8	-126.7	3.9	5	-1.18-	0.30	G5
	1366021	16.8	-0.1	319.9	40.8	305.3	2.3	7	-1.69	0.15	A2
P802/1	399824	17.4	0.8	339.2	32.6	-102.8	6.8	5	-1.50	0.24	G2
	377128	16.9	0.7	339.4	32.9	-56.3	3.7	8	-0.68	0.17	F8-GO
	365774	17.3	0.9	339.6	33.1	-55.4	1.6	3	-0.88	0.34	GO
	377153	16.5	0.9	339.5	33.0	-109.3	6.6	7	-1.35	0.29	G6
	388911	16.5	0.8	339.5	32.7	32.0	3.9	6	-0.59	0.15	F8
	399902	16.9	0.7	339.4	32.6	-1.2	6.0	4	-1.49	0.15	F8
	389096	17.1	0.9	339.6	32.6	69.7	5.7	7	-1.34	0.30	G5
	365722	17.5	1.0	339.6	33.1	59.1	6.6	6	-1.66	0.27	G5
	388988	17.5	1.0	339.5	32.8	158.0	2.4	4	-0.84	0.16	F8
	389033	16.8	0.5	339.7	32.7	200.3	5.0	4	-1.75	0.16	F6
	377449	17.0	0.8	339.6	32.8	166.3	6.0	4	-1.45	0.15	F2-F5
	376616	16.6	0.8	339.2	33.1	33.9	5.7	6	-0.24	0.17	F8
	377253	17.1	0.7	339.5	33.0	52.3	2.7	5	-1.02	0.21	F8
	399862	17.11	1.0	339.2	32.6	-121.9	5.1	7	-1.72	0.21	G8
	376745	16.5	0.8	339.4	33.1	-86.4	1.6	8	-1.03	0.28	GO
	399896	17.0	0.9	339.4	32.6	63.6	6.0	4	-1.20	0.28	G2

Table 4—Continued

Field [a] /Obs. Run	APS Star [b] Number	O Mag	$(O-E)$	$l[^\circ]$	$b[^\circ]$	V_{helio} km s^{-1}	σ_{helio} km s^{-1}	Number Lines	$[\frac{Fe}{H}]$ [c]	$\sigma_{[\frac{Fe}{H}]}$	Spec. Type
	376668	16.6	0.9	339.2	33.2	-46.1	8.7	5	-1.33	0.35	GO
	376996	16.7	0.9	339.5	33.0	-62.7	5.0	6	-0.65	0.25	GO
	365963	16.7	0.8	339.7	33.0	-56.5	13.4	3	-2.02	0.15	FO-F2
	388288	16.8	0.9	339.2	32.9	-38.5	5.3	4	-1.54	0.35	G8
	377079	16.8	0.8	339.4	32.9	-14.7	3.7	5	-1.15	0.15	F8
	388927	16.7	0.6	339.5	32.8	-38.8	6.3	5	-1.18	0.30	G8
	377227	17.1	0.9	339.5	33.0	18.6	0.7	6	-0.64	0.28	G2
	377294	17.0	1.0	339.6	32.9	35.5	4.1	5	-0.85	0.25	GO
	388545	17.2	0.9	339.4	32.9	-53.8	5.9	7	-1.28	0.15	GO
	399335	16.9	0.8	339.0	32.9	-54.8	1.7	6	-1.57	0.15	F8
	399589	16.4	0.9	339.1	32.8	-22.3	5.1	6	-1.69	0.15	F8
	389048	17.4	1.0	339.6	32.6	-34.3	5.5	5	...	...	GO
	389069	17.3	1.0	339.7	32.7	-62.1	4.4	8	-1.36N	0.27	G0
	388895	16.7	0.6	339.4	32.7	-40.8	6.6	7	-1.67	0.18	G5
	376765	16.7	0.5	339.4	33.1	-143.6	3.5	7	-1.57	0.15	F8-GO
	377389	16.6	0.7	339.6	32.9	-42.9	3.0	5	-0.64	0.28	GO-G2
	389132	17.2	0.9	339.6	32.7	-0.4	6.9	8	-2.98	0.15	G8
	376769	16.9	0.9	339.3	33.0	-67.5	5.1	5	-1.28	0.15	G2
	388641	15.9	0.7	339.4	32.8	-67.5	5.1	5	-1.28	0.15	GO
P802/2	388930	16.1	1.0	339.5	32.7	33.6	4.1	6	···	···	G8
	399973	16.4	0.8	339.4	32.7	19.8	4.4	6	···	···	G5
	365602	15.8	0.9	339.6	33.1	-41.2	2.7	10	···	···	G5
	388914	16.0	0.8	339.5	32.8	-81.6	4.9	6	···	···	F4
	365825	16.1	0.8	339.6	33.1	-47.0	4.3	5	···	···	GO
	377361	15.9	1.0	339.6	32.9	-116.3	4.4	6	···	···	GO-G2
	388535	15.9	0.9	339.4	32.8	-61.8	5.5	6	···	···	GO-G2
	377073	16.3	0.7	339.5	32.9	-129.6	5.7	7	···	···	GO
	388411	16.0	0.7	339.2	32.9	-88.6	2.9	5	···	···	GO
	365569	15.9	0.8	339.5	33.2	-30.5	4.8	5	···	···	GO
	376481	16.1	0.9	339.2	33.1	-108.8	6.8	4	···	···	GO
	377628	16.3	0.1	339.8	32.8	-33.3	3.1	6	···	···	A5

Table 4—Continued

Field [a] /Obs. Run	APS Star [b] Number	O Mag	$(O-E)$	$l[^\circ]$	$b[^\circ]$	V_{helio} km s^{-1}	σ_{helio} km s^{-1}	Number Lines	$[\frac{Fe}{H}]$ [c]	$\sigma_{[\frac{Fe}{H}]}$	Spec. Type
	400043	15.9	0.5	339.4	32.6	38.8	2.7	6	···	···	F8
	388249	16.2	0.7	339.0	32.9	51.3	3.4	7	···	···	G2
	377332	16.3	0.8	339.7	33.0	10.5	1.4	5	···	···	G8
	376832	16.2	0.7	339.4	33.1	168.2	4.6	5	···	···	G2
	365342	16.4	0.9	339.5	33.2	-17.6	2.5	7	···	···	G5
	388968	16.0	0.8	339.5	32.8	-48.8	5.7	5	···	···	G5
P802/1,2	365582	16.4	0.8	339.6	33.1	-64.2	1.7	6	-0.88	0.34	GO
	365796	16.9	0.8	339.6	33.1	59.3	1.7	5	-0.88	0.34	G2
	376745	16.5	0.8	339.4	33.1	-86.7	1.6	8	-1.03	0.28	GO
	376819	16.9	0.6	339.3	33.0	-115.6	2.4	7	-1.02	0.21	F8-GO
	377037	16.8	0.8	339.4	32.9	45.4	0.8	6	-0.64	0.28	GO
	377204	16.5	0.9	339.5	33.0	-46.1	3.9	7	-1.36	0.27	G2-G5
	377538	16.7	0.9	339.8	32.8	41.7	2.0	8	-1.20	0.28	GO
	388136	16.7	0.9	339.1	33.0	-37.7	2.8	4	-1.33	0.35	G8
	388184	16.3	0.8	339.1	33.0	-80.0	3.0	5	-0.84	0.29	G5
	388781	16.4	0.2	339.4	32.8	-149.4	5.1	5	...	...	A2-A3
	388993	16.5	0.9	339.5	32.7	26.3	2.8	7	-0.88	0.36	G8
	389078	16.4	0.8	339.7	32.7	-105.1	3.2	5	-1.34	0.30	G8
	399557	16.8	0.8	339.1	32.8	-59.4	1.6	5	-1.02	0.21	GO
	399608	16.7	0.7	339.1	32.7	-90.9	4.5	10	-1.51	0.29	G5
	400110	16.8	0.8	339.4	32.6	-107.7	3.2	6	-1.39	0.15	F8-GO
P855/2	254171	16.5	0.9	309.3	36.8	121.4	3.5	5	···	···	G2
	238452	17.0	0.5	309.5	37.1	118.1	5.8	3	···	···	F6
	253836	16.9	0.9	309.1	36.8	-22.7	5.4	3	···	···	GO
	238377	17.0	0.9	309.5	37.0	-32.6	3.4	4	···	···	G5
	254204	15.8	1.1	309.3	36.8	73.1	4.6	5	···	···	G5-G8
	269045	16.5	0.9	309.3	36.7	62.5	8.8	5	···	···	G2
	237884	16.4	0.7	309.0	37.1	72.9	4.2	4	···	···	F5
	254331	17.2	1.0	309.5	36.8	-23.2	4.7	5	···	···	G8
	238398	16.3	0.9	309.5	37.0	-32.0	6.6	5	···	···	G2
	238505	16.3	0.9	309.5	37.1	39.3	10.6	4	···	···	F8-GO

Table 4—Continued

Field [a] /Obs. Run	APS Star [b] Number	O Mag	$(O-E)$	$l[^\circ]$	$b[^\circ]$	V_{helio} km s^{-1}	σ_{helio} km s^{-1}	Number Lines	$[\frac{Fe}{H}]$ [c]	$\sigma_{[\frac{Fe}{H}]}$	Spec. Type
	254214	15.7	1.0	309.3	36.9	35.6	5.1	10	···	···	G5-G8
	254452	16.9	0.7	309.7	36.9	34.3	6.2	6	···	···	GO
	238263	16.7	0.8	309.4	37.1	34.7	5.1	5	···	···	GO
	253793	16.0	1.0	309.0	36.9	-72.3	7.4	9	···	···	GO
	253687	15.7	1.1	309.0	36.9	-7.7	2.0	5	···	···	G8
	238087	15.8	0.9	309.2	37.1	-63.7	6.0	8	···	···	F8-GO
	238431	16.2	1.0	309.5	37.1	-46.7	5.5	6	···	···	G5
	254467	16.0	0.9	309.7	36.8	36.5	6.0	4	···	···	GO
	222098	16.4	0.8	309.4	37.3	83.8	7.4	4	···	···	GO
	253927	16.5	1.0	309.1	36.8	79.7	2.6	7	···	···	G5
	254106	16.0	0.9	309.3	36.8	37.1	4.6	8	···	···	G2-G5
	254266	15.9	0.8	309.5	36.7	-27.1	6.6	6	···	···	G2-G5
	221820	16.3	1.0	309.2	37.3	-41.6	2.4	3	···	···	F8-GO
	222157	16.4	0.9	309.5	37.2	71.4	6.5	3	···	···	G2
	238527	16.1	0.8	309.7	37.0	19.6	3.9	5	···	···	G2
	238031	16.9	0.9	309.2	37.0	-120.8	4.9	6	···	···	G2
	222039	16.3	1.0	309.4	37.2	-34.6	4.4	9	···	···	G5
	221628	15.9	0.9	309.0	37.2	111.0	9.6	4	···	···	F8
	253942	16.0	1.0	309.2	36.9	-13.2	2.1	4	···	···	G2
	237797	16.3	1.0	309.0	37.0	-33.2	8.5	5	···	···	G2
	269207	16.5	1.0	309.3	36.8	-39.6	7.0	8	···	···	G8
P858/1	351413	16.9	0.8	329.2	31.8	-109.0	1.7	5	-1.75	0.16	F8
	319245	17.3	0.8	329.6	32.1	71.5	4.9	6	-2.09	0.15	F6
	336122	16.7	0.6	329.4	32.0	-7.9	11.5	4	-3.15	0.26	A8-FO
	351949	16.8	0.7	329.6	31.8	131.8	6.2	6	-1.02	0.21	F8-GO
	351544	16.6	0.6	329.4	31.8	-9.6	3.4	7	-1.73	0.39	G8
	336627	16.7	0.8	329.5	31.9	-52.9	1.9	4	-1.66:	0.27	G8
	302309	16.7	0.8	329.5	32.3	-41.3	3.9	5	-2.78	0.30	G8
	319588	16.8	0.5	329.7	32.0	85.4	8.1	4	-2.24	0.15	FO
	336657	17.5	0.8	329.7	31.9	-227.4	4.8	5	-1.75	0.15	F6-F8
	350994	16.7	0.9	329.1	31.8	-76.8	6.0	7	-1.52	0.27	F8-GO

Table 4—Continued

Field [a] /Obs. Run	APS Star [b] Number	O Mag	$(O-E)$	$l[^\circ]$	$b[^\circ]$	V_{helio} km s^{-1}	σ_{helio} km s^{-1}	Number Lines	$[\frac{Fe}{H}]$ [c]	$\sigma_{[\frac{Fe}{H}]}$	Spec. Type
	319469	17.4	0.4	329.6	32.1	140.3	0.7	4	-2.13	0.15	FO
	351455	17.6	0.5	329.2	31.8	-55.3	3.9	5	-1.54	0.15	F2
	335990	16.8	0.6	329.3	31.9	167.4	10.9	5	-1.84:	0.15	F2
	336746	16.9	0.9	329.6	31.8	36.5	6.4	6	-1.36	0.27	GO
	351614	17.0	0.8	329.4	31.7	-88.6	1.7	5	-1.35	0.29	GO-G2
	351158	17.3	0.4	329.2	31.7	-97.0	8.7	6	-1.67	0.18	GO
	318526	16.5	0.8	329.3	32.2	-46.7	4.2	6	-0.84	0.21	F8-GO
	318938	17.4	0.7	329.4	32.1	94.4	9.1	4	-0.85	0.25	GO
	351024	17.3	0.8	329.1	31.8	-17.3	2.9	5	-1.36	0.27	G5
	351346	16.8	0.8	329.2	31.8	-69.2	4.9	9	-1.35	0.29	G5
	301875	16.9	0.8	329.4	32.3	34.9	5.2	5	-2.19	0.18	GO
	336848	16.5	0.6	329.6	31.8	41.7	7.3	4	...	...	G5
	335904	17.4	0.6	329.3	32.0	-84.0	2.6	5	-0.65	0.25	GO
	319216	16.8	0.8	329.6	32.1	-102.6	10.1	5	-1.03	0.25	GO
	351079	17.2	0.9	329.1	31.8	73.5	6.0	4	-3.13	0.15	G2-G5
	319316	17.5	0.9	329.6	32.0	-45.4	2.3	5	-1.43:	0.17	GO
	335138	16.6	0.7	329.1	32.2	86.4	7.3	5	-2.18	0.15	GO
	350457	16.5	0.5	329.0	31.9	-126.9	8.0	4	...	...	A2-A5
	350960	16.5	0.5	329.1	31.9	-70.3	8.1	3	-1.98	0.15	F2
	336765	17.6	0.5	329.6	31.8	93.5	7.6	5	-3.01	0.32	F2-F5
	336549	16.9	0.7	329.5	31.9	-47.6	5.0	7	-2.18	0.15	G2
	351612	16.7	0.8	329.4	31.8	24.0	2.9	3	-1.58	0.20	F8-GO
	336546	16.5	0.8	329.4	31.9	-25.0	3.8	7	-1.94	0.33	G8
	336553	17.0	0.8	329.4	31.8	-29.5	3.5	5	-1.87:	0.16	F8
	336559	16.5	0.5	329.5	31.9	0.9	5.4	5	-1.58	0.20	F8-GO
P858/2	336091	16.0	0.9	329.9	32.9	-120.9	3.5	4	···	···	GO
	319384	16.3	0.7	330.0	32.7	-165.2	5.7	3	···	···	F8-GO
	336075	17.6	0.6	329.9	32.9	-127.5	7.1	4	···	···	G8
	319285	15.9	0.7	330.0	32.8	55.0	5.3	3	···	···	G5
	335691	16.5	0.9	329.8	33.0	-16.6	3.3	5	···	···	G2-G5
	335622	16.0	0.8	329.8	33.1	-16.1	5.2	5	···	···	G5

Table 4—Continued

Field [a] /Obs. Run	APS Star [b] Number	O Mag	$(O-E)$	$l[^\circ]$	$b[^\circ]$	V_{helio} km s^{-1}	σ_{helio} km s^{-1}	Number Lines	$[\frac{Fe}{H}]$ [c]	$\sigma_{[\frac{Fe}{H}]}$	Spec. Type
P858/1,2	318526	16.5	0.8	329.3	32.2	-46.9	3.5	6	-0.84	0.21	F8-GO
	335961	17.0	0.8	329.4	32.0	-65.1	1.4	5	-1.35N	0.22	GO
	336730	16.6	0.7	329.7	31.9	-40.0	2.9	5	-1.52	0.27	GO
	350364	16.5	0.8	329.0	32.0	-145.1	4.5	7	-0.88	0.36	GO
P913/1	169227	17.2	0.9	320.0	30.2	-85.0	8.1	5	-0.50	0.15	GO
	169335	17.3	1.0	320.1	30.1	-30.1	5.9	6	-0.50	0.15	GO
	169472	17.5	0.7	320.2	30.2	-36.7	4.6	5	-1.28	0.15	G5-G8
	169497	17.2	0.8	320.1	30.1	24.3	7.8	5	-1.51	0.29	G2-G5
	183728	16.6	0.7	320.2	29.9	-73.3	8.8	8	-3.17	0.15	G8
	183844	16.7	1.1	320.3	29.8	-66.2	4.9	8	-2.19:	0.25	G8
	183811	17.5	0.9	320.4	29.9	22.3	3.6	5	-1.85:	0.27	G2-G5
	169735	17.0	0.6	320.3	30.1	-42.2	4.5	8	-0.64	0.28	G5
	183855	17.0	0.9	320.4	30.0	-78.2	7.3	7	-1.48	0.33	G8
	168697	17.1	0.9	319.8	30.1	-32.3	4.2	7	-0.26N	0.33	G8
	197535	17.8	0.7	320.0	29.8	-35.4	2.5	8	...	...	G2-G5
	183936	17.9	0.6	320.3	29.8	201.0	6.8	5	-1.80N	0.15	F5
	168742	17.5	-0.2	319.8	30.2	360.2	10.4	4	...	...	A2-A3
	169045	17.1	1.1	320.0	30.2	-43.4	4.2	6	-1.69	0.40	G8
	168818	17.3	0.9	319.9	30.2	-48.6	12.3	5	0.01	0.18	F8-GO
	197409	17.0	0.9	320.0	29.7	-62.7	4.4	7	-0.69	0.15	F8
	169690	17.0	0.6	320.3	30.1	34.2	5.1	6	-0.55	0.15	G5
	169449	16.8	0.8	320.1	30.1	-33.2	4.8	5	-1.28	0.15	G5
	169309	16.9	0.9	320.2	30.2	-40.7	2.7	6	-1.03	0.40	G8
	197347	16.7	0.9	319.9	29.9	-16.1	3.7	5	-0.26:	0.33	G8
	168989	16.9	0.5	319.9	30.2	-74.0	8.7	4	-1.87	0.23	F8
	169851	17.9	0.4	320.3	30.2	-109.2	10.2	4	-1.34	0.15	F5
	184052	17.1	1.1	320.4	29.9	36.9	3.4	9	-2.65	0.15	G8
	197686	16.8	0.9	320.2	29.8	-36.6	4.2	6	-1.66	0.27	G2
	197784	17.2	0.9	320.2	29.8	-105.6	7.0	6	-1.94	0.20	G8
	169079	16.7	0.6	320.0	30.1	-25.4	2.2	3	-1.36	0.15	F5
	169874	17.1	0.7	320.3	30.1	46.0	4.9	4	-1.75N	0.24	G5-G8

Table 4—Continued

Field [a] /Obs. Run	APS Star [b] Number	O Mag	$(O-E)$	$l[^\circ]$	$b[^\circ]$	V_{helio} km s^{-1}	σ_{helio} km s^{-1}	Number Lines	$[\frac{Fe}{H}]$ [c]	$\sigma_{[\frac{Fe}{H}]}$	Spec. Type
	182971	17.3	0.8	320.0	30.1	-59.3	7.2	4	-3.13	0.30	G8
P913/2	196888	17.5	0.3	320.1	30.9	91.3	11.8	4	···	···	A2
	197075	17.5	0.7	320.2	30.9	68.6	5.9	5	···	···	G8
	183612	16.8	1.0	320.5	30.6	-47.9	9.0	8	···	···	G5
	197383	17.3	0.7	320.4	30.9	-120.6	5.6	4	···	···	F8-GO
	170063	15.8	0.9	320.5	30.4	-26.9	2.7	3	···	···	G8
	197003	17.6	0.8	320.2	30.9	76.0	3.3	4	···	···	G5
	183755	17.3	1.0	320.5	30.5	-50.2	5.0	5	···	···	G0
	197804	17.6	0.7	320.6	30.8	32.4	3.8	5	···	···	G5
	169205	17.1	0.9	320.1	30.4	-5.5	4.0	4	···	···	G5
	183557	16.5	0.7	320.4	30.6	69.5	8.7	7	···	···	F8
	169422	15.8	0.6	320.3	30.5	50.6	6.9	7	···	···	F8
	183892	16.8	0.9	320.6	30.6	118.6	10.9	5	···	···	G2
	168723	16.5	1.0	319.9	30.5	-35.8	5.0	6	···	···	G0
	168755	16.2	1.0	319.9	30.6	-27.4	6.5	5	···	···	G2
	197096	17.0	1.0	320.2	30.9	-73.8	11.3	5	···	···	G5
P913/1,2	169249	16.9	0.7	320.0	30.3	20.4	1.2	6	-0.46	0.35	G5
	169262	16.9	1.1	320.0	30.2	111.7	3.5	5	-1.20	0.28	G5
	169362	16.8	1.0	320.2	30.2	-41.8	2.5	11	-0.84	0.29	G8
	169562	16.7	0.6	320.2	30.2	38.9	6.4	6	-1.32	0.18	GO
	169971	17.1	1.1	320.4	30.0	-9.2	3.4	5	-3.03:	0.15	G8
	182937	16.7	1.1	319.9	29.9	-14.0	1.2	5	...	...	G8
	183247	17.4	1.0	320.1	30.0	-49.5	3.8	4	-9.99	-9.99	G8
	183612	16.8	1.0	320.2	29.9	-46.5	4.9	5	-0.13	0.27	G8
	196922	16.7	1.0	319.7	29.9	-32.2	4.8	6	-2.07:	0.15	G2-G5
	197176	16.8	0.7	319.9	29.8	91.5	5.9	5	-0.50	0.15	F8-GO
	197520	16.7	0.7	320.0	29.8	-111.7	5.0	6	-1.58	0.20	F8-GO
	197700	16.8	0.8	320.2	29.8	-72.7	2.4	10	-1.80	0.19	G8
	197743	16.9	1.0	320.1	29.7	-56.6	1.8	4	-1.18:	0.15	F2

[a]1, 2, 3 refer to the three observing runs CTIO 1999, CTIO 2000, and WIYN 2000 respectively.

[b]Positions for the stars can be obtained from the Minnesota Automat ed Plate Scanner(MAPS) Catalog of the POSS I using either the sql-based query for individual sta rs (http://aps.umn.edu/catalog/sql.html) or the skybox query ((http://aps.umn.edu/catalog) for a region on the sky.

[c]Stars with spectra considered too noisy to obtain reasonable abundance estimates have a ... as t heir [Fe/H] value and are not used in the measurement of the mean. Stars with inferred $(B-V)_0$ colors outside the "optimum range" are labeled with a ":". Stars with a noisy spectrum, but have an abundance estimate are labeled with a "N".

This figure "JParker_fig05.jpg" is available in "jpg" format from:

http://arXiv.org/ps/astro-ph/0312017v1

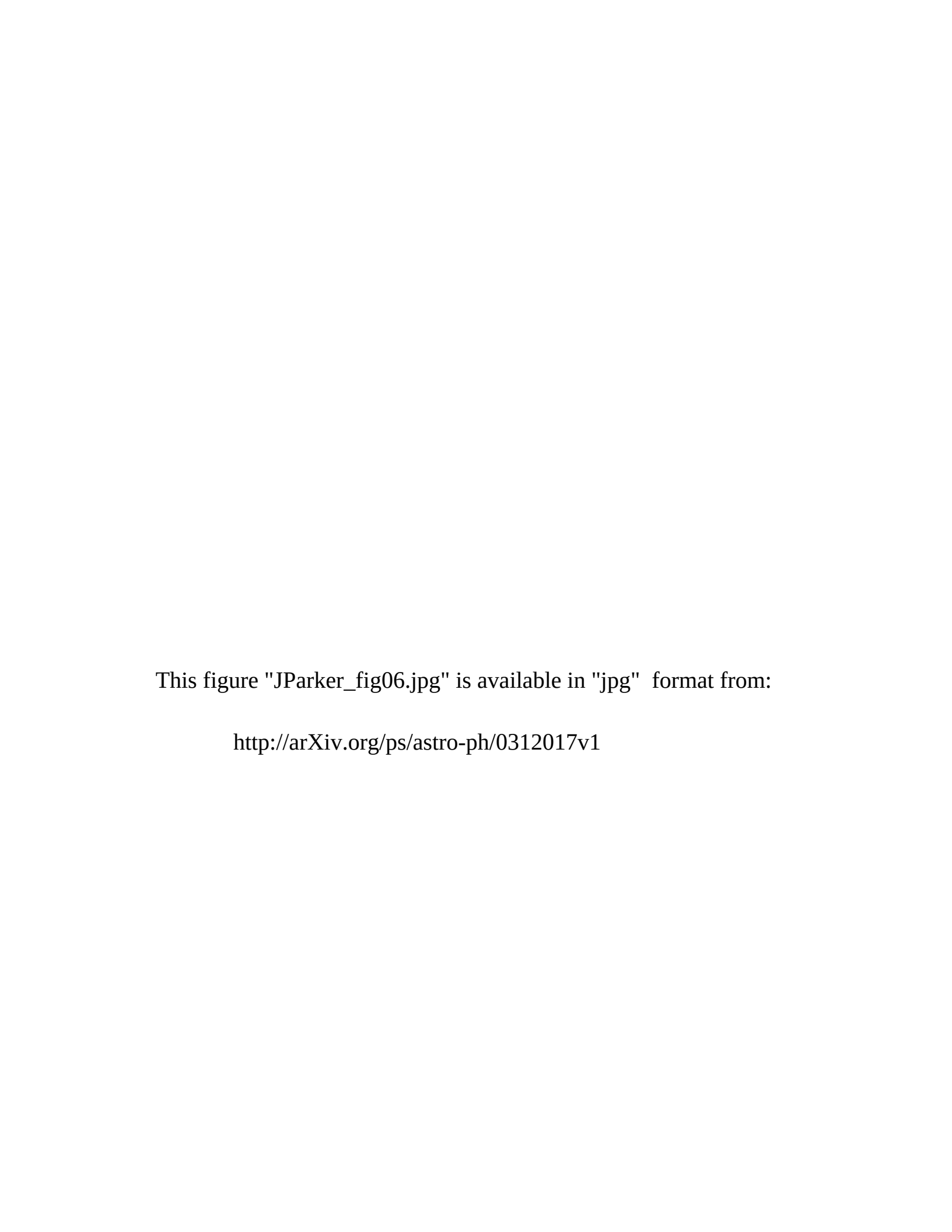
This figure "JParker_fig06.jpg" is available in "jpg" format from:
http://arXiv.org/ps/astro-ph/0312017v1

This figure "JParker_fig07.jpg" is available in "jpg" format from:

http://arXiv.org/ps/astro-ph/0312017v1

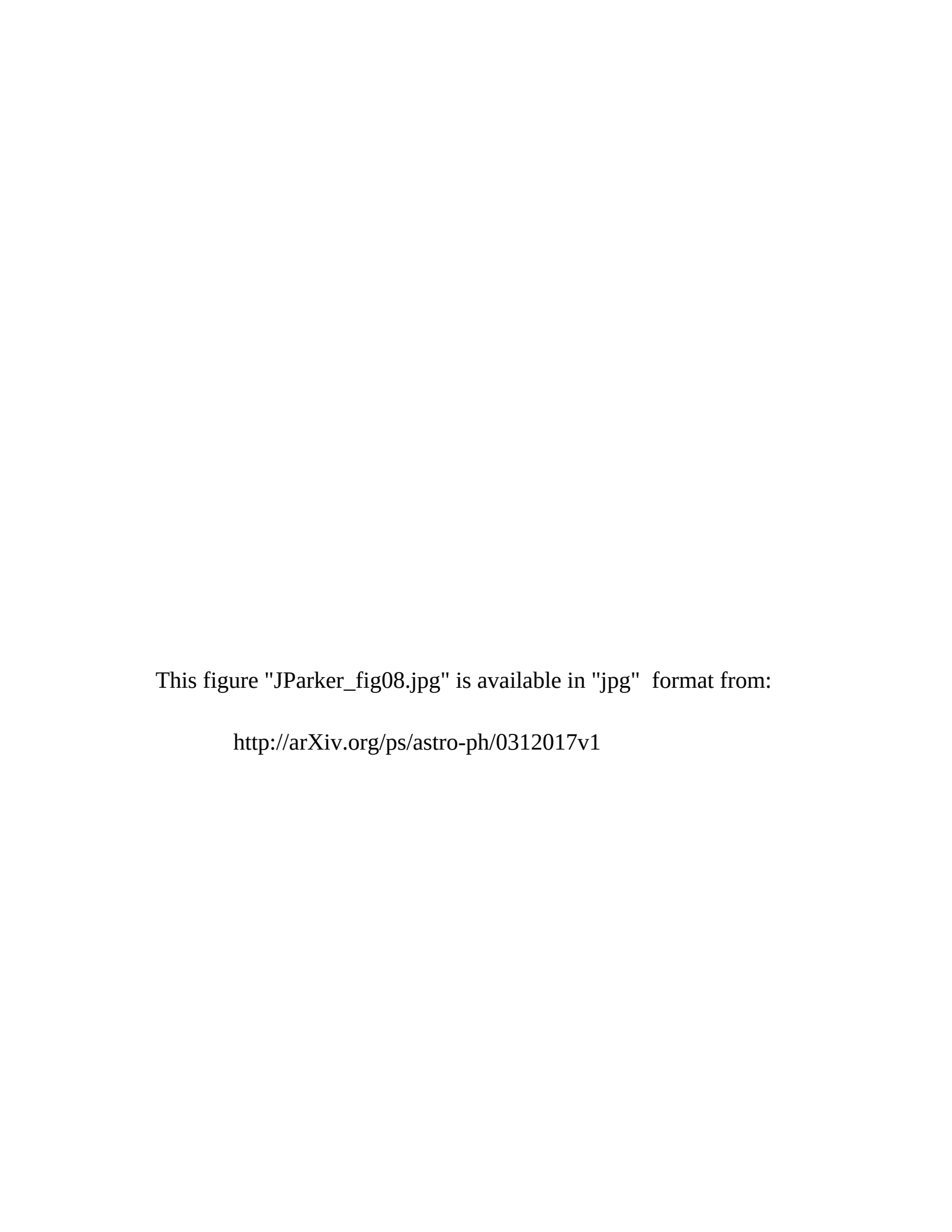
This figure "JParker_fig08.jpg" is available in "jpg" format from:
http://arXiv.org/ps/astro-ph/0312017v1